Full Length Article

Tribological and radiation shielding response of novel titanium-boron nitride coatings for lunar structural components

Abhijith Kunneparambil Sukumaran [a], Cheng Zhang [a], Sara Rengifo [b], Michael Renfro [c], Gia Garino [a], William Scott [b], Matthew Mazurkivich [b], Annette Gray [b], Gabriel Demengehi [d], Ellen Rabenberg [d], Martin Volz [d], Malik Thompson [e], Brandon Phillips [d], Nathan Jimenez [f], Felipe Mora [g], Calista Lum [h], Katie Stephens [i], Sang-Hyon Chu [j], Cheol Park [j], Arvind Agarwal [a,*]

[a] Plasma Forming Laboratory, Florida International University, Miami, FL, United States of America
[b] Materials Test, Chemistry and Contamination Control Branch, National Aeronautics and Space Administration Marshall Space Flight Centre, Huntsville, AL, United States of America
[c] Plasma Processes, LLC, Huntsville, AL, United States of America
[d] Materials Diagnostics and Fracture/Failure Analysis Branch, National Aeronautics and Space Administration Marshall Space Flight Centre, Huntsville, AL, United States of America
[e] Nonmetallic materials and space environmental effects branch, National Aeronautics and Space Administration Marshall Space Flight Centre, Huntsville, AL, United States of America
[f] Structural Mechanics Branch, National Aeronautics and Space Administration, Glenn Research Center, Cleveland, OH, United States of America
[g] Modal Dynamics Test Branch, National Aeronautics and Space Administration Marshall Space Flight Centre, Huntsville, AL, United States of America
[h] University of California, Irvine, Irvine, CA, United States of America
[i] University of California, Merced, Merced, CA, United States of America
[j] Advanced Materials and Processing Branch, NASA Langley Research Center, Hampton, VA, United States of America

ARTICLE INFO

ABSTRACT

Aluminum (Al) and titanium (Ti) lightweight alloys play a crucial role in space systems due to their exceptional strength-to-weight ratio. However, their premature failure in the presence of lunar regolith and their lack of neutron shielding ability are significant challenges. To address these issues, we have developed air and vacuum plasma-sprayed hBN (hexagonal Boron Nitride) -reinforced titanium coatings with 2 and 10 vol% of hBN. Tribological studies conducted with JSC-1 A lunar regolith simulant revealed a 90 % reduction in wear volume for the Ti/2 vol% hBN coatings compared to conventional materials due to the synergistic action of harder secondary phases and solid lubrication effect of hBN. Additionally, a 27 % enhancement in radiation shielding is obtained based on the mass absorption coefficient (radiation absorbed per sample density and thickness) for VPS Ti/2 vol% hBN coatings.

1. Introduction

Al6061 and Ti6Al4V are important for lunar structural components due to their high specific strength, workability, and excellent corrosion resistance [1–13]. Rover frames, wheels, grousers, bearings, seals, etc., are made out of these alloys [6,7,14–22,70,72]. However, the life of these alloys deteriorates rapidly upon exposure to harsh lunar environments such as extreme vacuum, prolonged thermal cycles, solar and intergalactic cosmic radiation, and abrasive lunar regolith [23–30]. The regolith particles have sharp edges and bi-modal particle size distribution due to the lack of erosion by water and wind [31,32]. The highly

abrasive nature of these particles causes catastrophic damage to the alloys when rubbed against or in between two parts. In addition, the high-velocity regolith impact during the ascent and descent of lunar landers results in erosive wear [33–35]. Furthermore, the lack of atmosphere and magnetic field on the lunar surface enables harmful space radiations such as galactic cosmic rays (GCR), solar particle events (SPE), and secondary albedo (radiation reflected off the surfaces) radiation to pass through to the lunar surface [29,36]. Exposure to these radiations for a prolonged period results in brittle fracture and failure of structural systems and microelectronics [37,38]. Hence there is a need to develop novel materials that can enhance both wear resistance and

radiation properties to improve the durability of aerospace structural components.

A novel multi-functional hexagonal boron nitride-reinforced composite coating is proposed in this study to improve the wear and radiation resistance of Al6061 and Ti6Al4V. Hexagonal boron nitride is well-known for its excellent thermal, tribological, and radiation shielding properties. hBN has high thermal conductivity (550 W/mK), low friction coefficient (0.1–0.7), and high wear resistance [39,71]. hBN has a similar atomic structure to graphene, made up of B and N elements, held together by strong covalent bonds in-plane and weak Van der Waals forces between planes. This layered structure shears off upon each other in sliding and reduces friction during abrasive contact. The boron element in hBN has the highest thermal neutron absorption cross-section (~760 b), 20 times more than graphene and 500 times more than conventional shielding material concrete [40].

Several studies have used hBN as a solid lubricant in composite coatings and nanocomposites to minimize friction and wear in harsh operating conditions. Ni_3Al-hBN composite coatings prepared by atmospheric plasma spraying (APS) have improved the friction coefficient by 50 % and wear rate by 66 % for 10 wt% hBN as compared to pristine Ni_3Al coating. This study reveals that when hBN content is <10 wt%, solid lubrication dominates over fracture and wear, while adding above 10 wt% causes weakened bond strength and increased wear loss [41].

NiCr-hBN composite coating, produced via APS at 500 °C, reduced the coefficient of friction (COF) by 30 % [40]. Ti6Al4V composite coatings, with 15 wt% BN reinforced powder, form in-situ TiB-TiN phases for implants [41]. The coating microhardness of 855 HV is seven times greater than pure Ti, resulting in an in vitro wear rate ($2.4 \times 10–5$ mm^3/Nm), an order of magnitude lower compared to pristine samples. Also, spark plasma sintered Boron Nitride Nanotube (BNNT) -reinforced Ti composites exhibited 26 % improved wear volume and 50 % enhanced neutron shielding with 1 wt% BNNT [42]. hBN has also been incorporated in polymer nanocomposites to enhance the radiation shielding capacity in aerospace applications. A multilayer polyethylene/hBN composite fabricated by hot pressing has shown high neutron shielding efficiency of up to 40 % for 30 wt% hBN and excellent thermal conductivity that benefits heat dissipation forming during neutron collision [42]. However, the synergetic improvement in wear and radiation shielding properties of BN-reinforced coatings has not been studied yet.

The present study aims to reinforce hBN to titanium matrix to enhance the tribological and radiation shielding properties of lunar structural components. Ti/ 2 vol% hBN and Ti/ 10 vol% hBN composite coatings were produced by atmospheric and vacuum plasma spray (APS and VPS) methods on Al6061 and Ti6Al4V substrates. The cryo-milling technique facilitated the uniform distribution of hBN particles in Ti6Al4V powder. The feasibility of Ti-hBN coating as a multi-functional
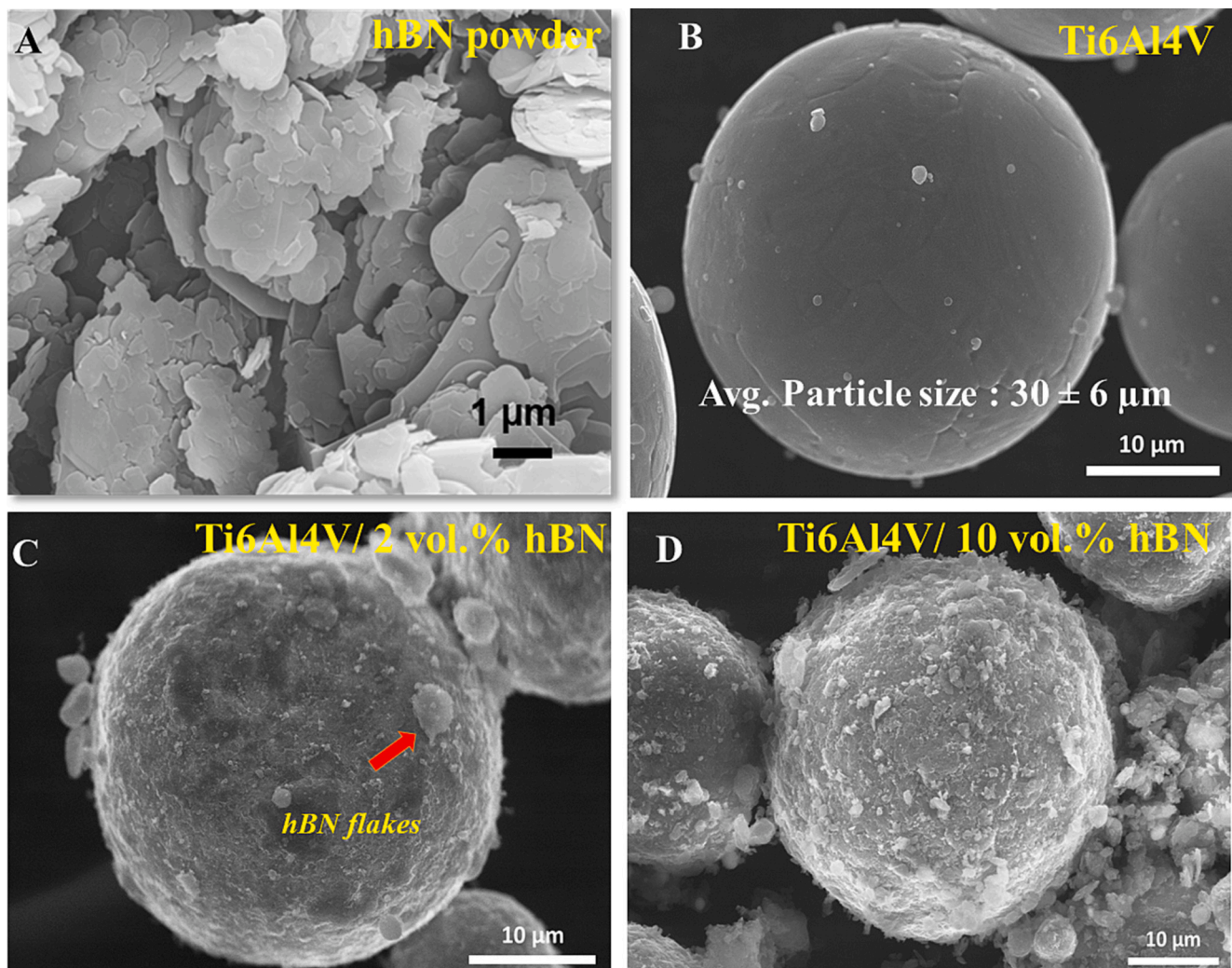

Fig. 1. SEM images of (A) as-received hBN powder, (B) as-received Ti6Al4V powder, (C) Cryo-milled Ti6Al4V/2 vol% hBN powder with well dispersed hBN flakes on Ti6Al4V powder, and (D) Cryomilled Ti6Al4V/ 10 vol% hBN powder with agglomeration and interparticle sticking. The powder feed rate into the plasma plume decreases from B—D to 28 g/min, 22 g/min, and 14 g/min, respectively.

protective material for harsh aerospace conditions was evaluated after extensive tribological and radiation testing.

2. Experimental details

2.1. Materials and preparation

To prepare composite Ti-hBN powder for plasma spray, hBN powder Fig. 1A (average particle size of 5 μm, surface area = 7.5 m^2/g, density = 2.1 g/cm^3, graphene supermarket) was mixed with Ti6Al4V powder (average size <30 μm, density = 4.5 m^2/g, Tekna TEKMAT™ Ti64–45/16-G5) metal powder Fig. 1B and subjected to a cryo-milling process. The composite powders were prepared at Ti6Al4V/ 2 vol% hBN and Ti6Al4V/ 10 vol% hBN concentrations. Two grinding bowls (250 ml) and a mixture of two types of grinding balls (each diameter, 0.51 cm and 1.91 cm) were used to obtain a uniform mixing and retain the spherical morphology of metal particles. The ball mass (M_B) to powder mass (M_P) ratio (M_B/M_P) was selected as $M_B/M_P = 10$ for the planetary ball mill processes. The pre-mixing process of hBN and Ti6Al4V powders was implemented in the glove box filled with argon gas (< 58 ppm O$_2$) to avoid surface oxidation. Furthermore, to minimize the deformation of metal particles, excessive heat generation, and facilitate uniform dispersion of hBN reinforcement, the entire set of two bowls containing two types of grinding balls and the hBN-metal powder mixtures were cooled down to a cryogenic temperature at -97 °C in liquid nitrogen, before the high-energy ball mill process. The powders were cryo-milled for 15 min and then retrieved by removing the grits using a No. 30 sieve (600 μm mesh size).

Conventionally manufactured (CM) Al6061 and Ti6Al4V machined to Φ 3.81× (t) 0.64 cm circular pucks were used as substrates for APS and VPS coating deposition. Substrates were cleaned using acetone and sandblasted with 54-grit alumina at 40 psi for 5 min to ensure proper surface roughness and integrity for coating adhesion. Then, the substrates were preheated with one pass of plasma plume before feeding in the powders to minimize the CTE (coefficient of thermal expansion) mismatch and to eliminate thermal stresses, cracks, and delamination. APS coating deposition was conducted at the Plasma Forming Laboratory of Florida International University, while VPS coatings were deposited at Plasma Processes, LLC in Huntsville, Alabama. SG-100 plasma gun (Praxair Surface Technologies, Indianapolis, Indiana) was used for coating deposition. All coatings were deposited to have a minimum thickness of 150 μm. The detailed process parameters of the coating deposition are provided in Table 1.

2.2. Composite powder and coating characterization

The powder feed rate and flowability are critical for a successful thermal spray process. The powder feed rate was measured by flowing the powder through the feeder tube into a collection bottle using carrier gas for 1 min. The weight of the collected powder was measured using a weighing balance precise to 0.01 mg.

The microstructural analysis of the raw powders and as-sprayed coatings was performed using a Schottky field emission scanning electron microscope (FESEM, JEOL-F100, JEOL Ltd., Tokyo, Japan) for morphological features and particle size distribution. The particle size distribution was quantified using ImageJ software. The as-sprayed coatings were sectioned, cold mounted in epoxy resin, and ground down to 1200 grit SiC paper. Polishing was done using 1 μm alumina

suspension and 0.05 μm colloidal silica suspension for microstructural characterization. The microstructure and cross-sectional analysis of the coatings was performed using SEM with a secondary electron detector and backscatter detector equipped with EDS. The composite coatings' thickness and area percentage porosity were quantified from ImageJ analysis. Ten random images of the coatings across the polished cross-sections have been analyzed, and the results were averaged to obtain the thickness and porosity.

The structure and phase fractions of the as-sprayed coatings were analyzed using X-ray diffraction (XRD, Rigaku Smart lab) using λ(Cu Kαl =1.54 Å) at a scan rate of 2°/min. The operating voltage of 40 kV and current of 40 mA was set in the 2θ range of 10° to 90°. The phase fractions were further deduced by Rietveld refinement. Identification of chemical compositions and secondary phases in the coatings was also analyzed using Raman spectroscopy at Langley Research Center, Hampton, Virginia (Thermo Scientific DXR2 Raman microscope system) equipped with a laser excitation of 532/785 nm under 50× objective lens. The spectral background was corrected using a smart subtraction offered by the Raman microscope.

The hardness of the as-sprayed coatings was measured using a Vickers microhardness tester (LM810AT, LeCO, USA). An indentation load of 100 gf was used with a dwell time of 15 s. At least ten indentations were conducted across the polished cross-section to obtain the average microhardness. Samples were mounted in resin and polished up to 0.05 μm surface finish before the hardness measurement.

2.3. Tribological testing

The tribological properties of the coatings were carried out using a ball-on-disk tribometer in two different conditions: with and without JSC-1 A lunar mare simulant. JSC-1 A represents the darker mare regions of the Moon, which are rich in silica, iron oxide, alumina, magnesium oxide, and calcium oxide. The simulant particles were fed continuously between the contact pair for the entire test duration. The detailed test parameters are given in Table 2. The wear test parameters were chosen to replicate the abrasive conditions of the lunar environment and based on previous lunar regolith abrasion studies. The literature on previous lunar regolith abrasive studies on similar materials has employed a load range of 5-10 N [43–45]. The 9 N load ensures that the contact pressure generated between mating parts is similar to the applied pressure of lunar/martian rovers, rims, sprockets, and grousers [15,17,18,20,46–48]. The acting contact pressure for the experiment was calculated using Hertzian contact pressure generated between the mating surfaces defined as [49].

$$P\,max \cong 0.4 \left(\frac{E^{*2}F}{R^2} \right)^{1/3} \tag{1}$$

where E is the effective elastic modulus of contacting surfaces, R is the radius of the contacting sphere, and F is the applied load. For mating

Table 2
Ball-on disk test parameters.

Counter Surface	Counter surface diameter (mm)	Load	Speed	Wear Scar Diameter	Duration
SS440C	5 mm	9 N	0.021 m/s	8 mm	30 min

Table 1
Plasma spray process parameters.

Process Type	Spray distance (mm)	Feeding Type	Primary gas pressure (psi)	Secondary gas pressure (psi)	Carrier gas pressure (psi)	Plasma power (kW)	Deposition time (min)	Vacuum level (Torr)
APS	140	External	40(Ar)	80(He)	30(Ar)	22	1.5	NA
VPS	100	External	100(Ar)	50(He)	35(N$_2$)	24	1.5	500

pairs, the contact pressures were calculated as SS440C- Al 6061: 975 MPa and SS440C-Ti6Al4V: 1220 MPa. The tests were done in 30 min to ensure proper wear quantification at longer durations, where simulants get fractured and fragmented during repeated sliding.

The mass loss from the coatings was measured using a balance with a precision of 0.1 mg. The profile of wear tracks and volume losses were calculated using a non-contact surface profilometer (Keyence VK-X 1100) with confocal microscopy. The wear volume was obtained by averaging five distinct wear profiles (wear width, depth, and area) from the wear scar profilometry. The specific wear rate was calculated using Eq. (1) [50].

$$Ws = \frac{V}{F \times L} \qquad (2)$$

where W_S is the specific wear rate (mm^3/Nm), V is the total friction volume (mm^3), F is the normal load (N), and L is the overall sliding distance (m).

2.4. Radiation shielding testing

The neutron radiation shielding testing was conducted at NASA Langley Research Center to test various samples. For neutron activation, a circular piece of pure indium (In) foil with a diameter of 25 mm and a thickness of around 1.0 mm was used as a reference target to be activated with or without a sample. The In foil was exposed to a one-Curie Americium (241Am)-Beryllium (9Be) neutron source through the shielding material in the test, as shown in Fig. S1A. To moderate the neutron emission, a polyethylene (PE) block of around 2.5 cm thickness was placed in front of the Am—Be neutron source to slow down the fast neutrons (4.5 MeV) from the Am—Be source (1 Ci). The dose rate of neutrons was decreased from 800 mrem/h to 320 mrem/h by the PE block moderator. The In foil and test material set was placed behind the PE block and exposed to neutron irradiation at a dose rate of 320 mrem/ h so that the 115In could be activated to 116In by neutrons. The set of In foil and test samples was exposed overnight (over 6 h) to reach the saturation activity of the neutron activation over 99 % for the activation equilibrium. On the next day, the activated In foil was removed from the test sample and counted using a Geiger-Mueller (GM) meter (Spectrum Techniques, GM35 Geiger-Mueller tube) with a digital counter (Spectrum Techniques, ST360 counter). The neutron shielding effectiveness was determined by the linear absorption cross-section (or coefficient, μ_x) and mass absorption cross-section (or coefficient, μ_m) of the material. Both coefficients can be calculated using the following equations:

$$\mu_x = -\frac{1}{t} ln\left(\frac{A}{A_0}\right) \qquad (3)$$

$$\mu_m = \frac{\mu_x}{d} \qquad (4)$$

where t is the sample thickness, d is the sample density, A_o is the average initial activity of unshielded In foil, and A is the average initial activity of shielded foil. In addition to experimental studies, NASA Langley Research Center developed the Online Tool for Assessment of Radiation in Space (OLTARIS) to model the coating samples under space radiation environments. The space radiation shielding effectiveness of the samples was modeled under GCR, using NASA Langley's deterministic transport code, HZETRN (High Z and Energy TRanNsport), based on the Boltzmann transport equation. The web-based OLTARIS allowed utilizing the newest version of HZETRN and the nuclear physics model, such as NUCFRG2 (NUClear FRaGmentaion2), to improve the contributions from secondary nuclear fragmentations of nucleons and light ions. For space radiation environments provided by OLTARIS, the Badhwar-O'Neill (BON) 2020 spectrum was selected for the GCR model and used for free space.

3. Results and discussions

3.1. Characterization of powders

The powder morphology of the as-received powders and cryo-milled composite powders are given in Fig. 1. The hBN micro powder has a flake-like structure with an average particle size of 5 ± 2 μm (Fig. 1A). The pristine Ti6Al4V powder has a spherical morphology with an average particle size of 30 ± 6 μm (Fig. 1B). The composite Ti/2 vol% hBN powder retains the spherical shape of the feedstock Ti6Al4V powder. It is covered with an even layer of hBN particles due to cryo-milling. hBN flakes can be seen sitting on top of the Ti6Al4V powder particles due to the cold welding by milling. It shows that uniform dispersion of hBN particles was obtained after the cryo-milling with 2 vol% hBN without the formation of heavy agglomerates and inter-particle sticking (Fig. 1C). In contrast, the Ti/10 vol% hBN powder shows excessively deformed powder morphology with interparticle sticking due to agglomeration resulting from high hBN concentration (Fig. 1D).

The change in powder morphology, with the addition of hBN, reduced the powder flowability and feed rate for composite powders. The high flowability of pristine Ti6Al4V powder (28 g/min) was reduced to 22 g/min with 2 vol% hBN and decreased to 14 g/min with 10 vol% hBN concentration. This was attributed to the interparticle cohesion between particles from hBN agglomeration during powder dispersion. The reduction in powder flowability is expected to influence the microstructure, hardness, and tribological characteristics of the coatings after plasma spraying.

3.2. Microstructure and porosity of the coatings

Fig. 2 exhibits the backscattered electron cross-section images of the APS Ti/2 vol% hBN and Ti/10 vol% hBN (Fig. 2 A-D) and VPS Ti/2 vol% hBN and Ti/10 vol% hBN (Fig. 2 E-H) coatings on Al6061 and Ti6Al4V substrates. The APS and VPS Ti/2 vol% hBN coatings' microstructure is denser and devoid of microcracks and defects, ensuring good coating integrity and interfacial adhesion with the substrate materials. The number of unmelted particles retained in the coatings across the cross-section (see Fig. 2 A-B and E-F) and the top surface (see Fig. S2 A-B) after spraying is minimal, guaranteeing uniform melting of individual powder particles in the plasma plume and enhancing the interlayer strength in the coatings. In contrast, the microstructure of Ti/10 vol% hBN coatings contains defects such as unmelted particles in both cross-section as well as top surface (see Fig. 2C-D, G-H and Fig. S2C—D), microcracks propagating from the substrate to the surface, coating chipping at the top edges and isolated areas of delamination. The chipping and delamination are primarily observed in the APS coatings due to the higher concentration of hard secondary phases due to the reaction in atmospheric conditions. These secondary phases, distinct from porosities, manifest as discernible black features in the BSE SEM images of the coatings, particularly notable in APS coatings (Fig. 2A-D), arising from the interaction between titanium and atmospheric oxygen during plasma spray (Fig. 2I).

Multiple secondary phases can be identified from the coating microstructure attributed to the reaction between Ti6Al4V and hBN powder in the plasma plume for both APS and VPS coatings. In addition, the effect of atmospheric oxygen in the APS process also induces the formation of secondary oxide phases in the coatings. The presence of defects and secondary phases can enhance the porosity in the coating and deteriorate the overall coating strength.

The thickness and porosity of the as-sprayed coatings are provided in Fig. 3. The coating passes were adjusted to obtain a minimum thickness of 150 μm for all sprayed samples. APS and VPS Ti/2 vol% hBN coatings exhibit low porosity of <1 % and high densification due to better powder flow and less agglomeration between powder particles. Increasing the hBN concentration to 10 vol% significantly increases the porosity of APS coatings to 5–7 % due to hBN agglomeration, reduction
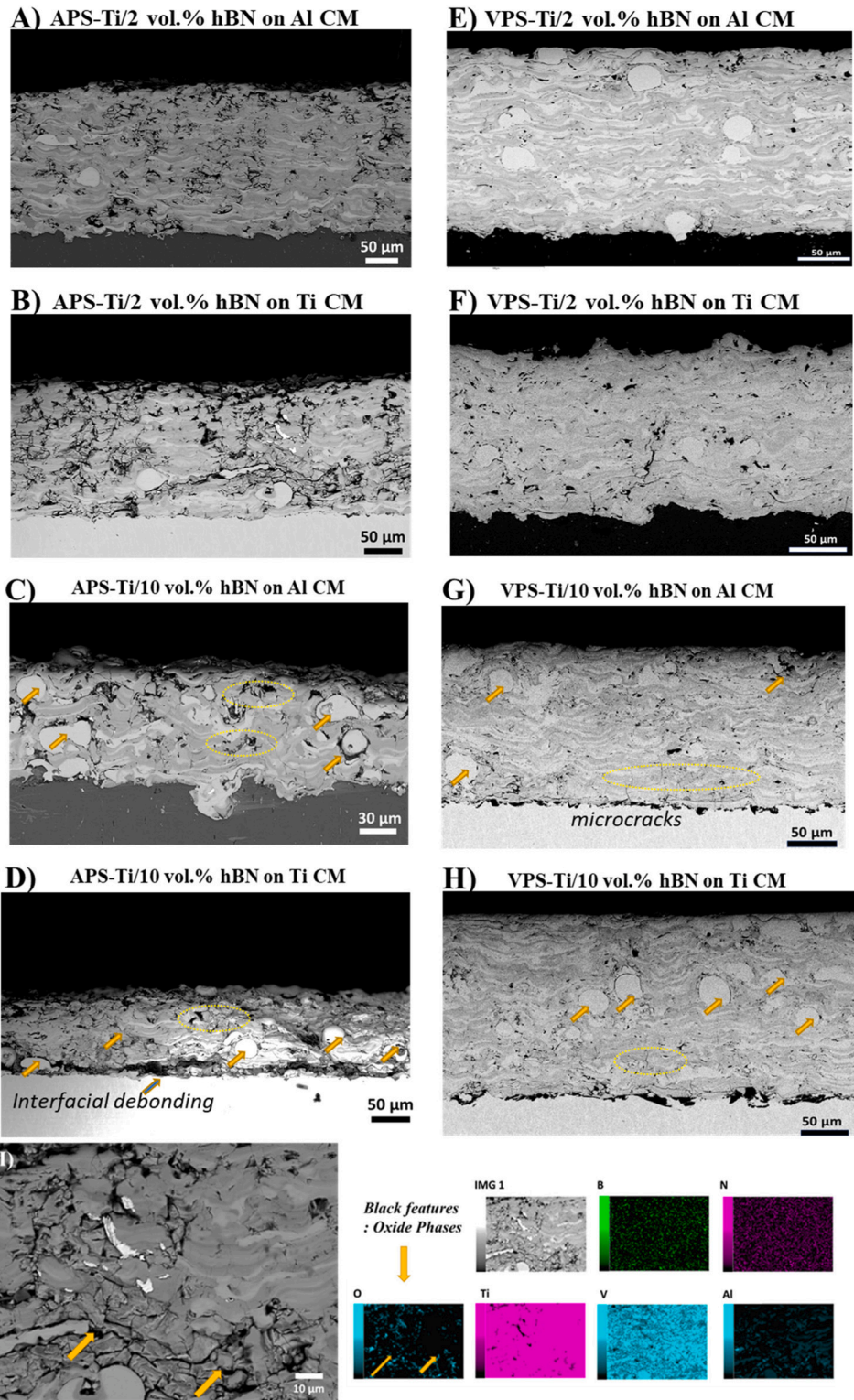
Fig. 2. SEM images of the plasma-sprayed composite coatings: (A) APS Ti/ 2 vol% hBN on Al CM, (B) APS Ti/ 2 vol% hBN on Ti CM, (C) APS Ti/ 10 vol% hBN on Al CM, (D) APS Ti/ 10 vol% hBN on Ti CM, (E) VPS Ti/ 2 vol% hBN on Al CM, (F) VPS Ti/ 2 vol% hBN on Ti CM, (G) VPS Ti/ 10 vol% hBN on Al CM, and (H) VPS Ti/ 10 vol% hBN on Ti CM. The yellow arrows indicate unmelted particles and porosities, the yellow oval shows microcracks and porosities, and the blue arrow shows interfacial debonding. (I) Black features in the high magnification image of Ti/2 hBN APS coating indicate the TiO phase as per EDS analysis.

in powder feed rate, and increase in the number of unmelted particles and inclusions. During APS, the air resistance reduces the in-flight velocity of powder particles, which decreases the impact force and leads to rapid solidification and smaller deformation of melted particles [51]. As a result, the pore appears particularly around semi-melted or unmelted particles. In addition, the surface oxidation of the melted particles increases the porosity between lamellar structures [51]. However, even with higher hBN content, the porosity is below 1 % for VPS coatings, owing to vacuum spraying conditions. Still, the reduction in powder feed rate at high hBN concentration increases the number of unmelted
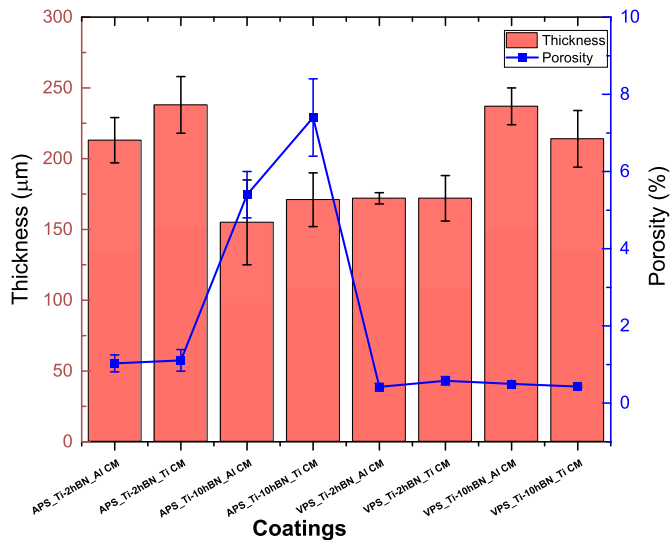
Fig. 3. Thickness and porosity of the plasma-sprayed composite coatings.

particles in the coatings, as seen in Fig. 2G-H.

3.3. Phase analysis of the composite coatings

The X-ray diffraction patterns of the composite powders and as-sprayed coatings are shown in Fig. 4A. For the composite powders, the presence of hBN was found only in the 10 vol% hBN concentration, possibly due to the low percentage of hBN in the 2 vol% hBN coatings. The major phases identified in the as-sprayed composite coatings are unreacted Ti and TiO. The presence of hBN was not identified from XRD patterns for both APS and VPS Ti/2 vol% hBN coatings, possibly due to the minuscule concentration of hBN and the high chances of chemical reactions between hBN and Ti6Al4V powder in the plasma plume. Minor peaks of hBN were found at $2\theta = 26.7°$ for Ti/10 vol% hBN APS and VPS coatings.

Other secondary phases, such as TiO_2, TiN, TiB, and TiB_2, were not identified from the XRD analysis, probably due to the low phase fraction of these formed phases, or they can be in amorphous form due to the rapid cooling nature of plasma spray. Upon interaction with the plasma plume, the cryo-milled composite powder is expected to undergo several chemical reactions, such as,
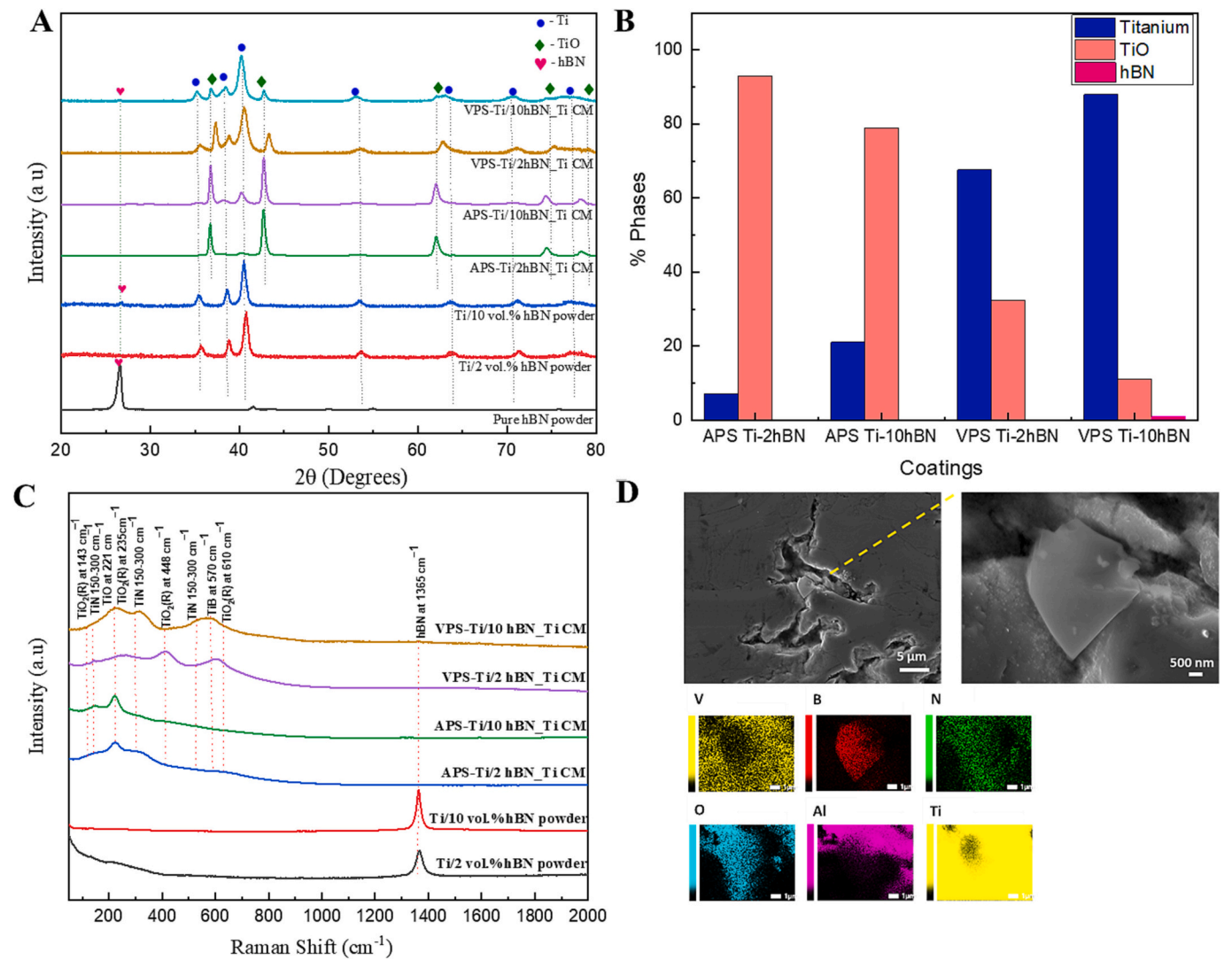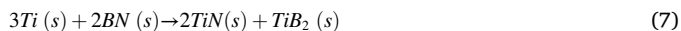

Fig. 4. (A) X-ray diffraction pattern of the composite Ti6Al4V/hBN powders and as-sprayed coatings (B) percentage phase fraction quantified from Rietveld refinement (C) Raman spectrographs of the composite Ti6Al4V/hBN powders and as-sprayed coatings (D) EDS map analysis of APS Ti/2 vol% hBN coating showing the presence of hBN in the coating cross-section.

$$Ti\ (s) + (1/2)\ O_2(g) \rightarrow TiO(s) \qquad (5)$$

$$Ti\ (s) + O_2(g) \rightarrow TiO_2(s) \qquad (6)$$

$$3Ti\ (s) + 2BN\ (s) \rightarrow 2TiN(s) + TiB_2\ (s) \qquad (7)$$

$$2Ti\ (s) + BN\ (s) \rightarrow TiN(s) + TiB\ (s) \qquad (8)$$

The plasma plume temperature may vary significantly and exceed 10,000-15,000 K, depending on plasma gas, voltage, and current. However, powder particles do not achieve such high temperatures due to short residence time (order of milliseconds) in the plume. Multiple studies [52–54] on in-flight particle diagnostics of Ti-based alloys at processing parameters similar to our experimental conditions showed an in-flight particle temperature of ~2000 K. Factsage predictions on Gibbs free energy (ΔG) of the reaction products from Eqs. (4) to (7) at particle temperature of 2000 K were calculated as −362.37, −589.61, −399.23, and − 227.68 kJ, respectively. This shows $\Delta G_{(6)} < \Delta G_{(5)} < \Delta G_{(7)} < \Delta G_{(6)} < 0$, meaning both Ti oxides and nitrides should form spontaneously thermodynamically. However, TiO is the predominant phase, compared to TiO_2, because the reaction between particles and oxygens is incomplete because of higher cooling rates, and the intermediate/metastable oxides will be produced faster [55]. TiO is usually an unstable phase, readily oxidizing to titanium dioxide in interaction with oxygen [56]. For VPS coatings, oxygen availability is limited to transform TiO to TiO_2. While for APS coatings, the stand-off distance between the plasma plume and substrate is small, the particles spent only a short residence time in the plasma plume at high temperatures, followed by very fast cooling rates (10^5–10^6 Ks^{-1} range) after impacting the substrate [57]. Hence, it results in the rapid formation of TiO rather than TiO_2. The phase fraction quantitated using the Rietveld refinement method is shown in Fig. 4B. For APS coatings, TiO has the highest phase concentration, with 90 % for Ti/2 vol% hBN coatings, which reduces to 80 % with a higher concentration of hBN due to the possible secondary phases formed in the reaction between Ti and BN. The concentration of the TiO phase reduces significantly to 35 % and 15 %, respectively, for the VPS 2 and 10 vol% hBN coatings, and the VPS Ti/10 vol% hBN shows a minuscule amount of 3 % hBN phase fraction.

Raman spectrographs shown in Fig. 4C identify reaction products such as TiO_2, TiN, and TiB. Raman peaks related to TiN_x (two broad bands at 150–300 cm^{-1}) [58] and TiO_2 (rutile, 610, 448, 235, and 143 cm^{-1}) [59] were observed for APS Ti/2 vol% and 10 vol% hBN- samples because of chemical reactions between Ti and BN and oxidation reactions during plasma spray. As per Raman spectroscopy, no definite hBN peaks were identified from Ti/2 vol% hBN APS and VPS coatings, possibly due to reactions (6) and (7). According to Raman, spectra collected from multiple locations of VPS Ti/10 vol% hBN coating revealed the presence of hBN (at ~1365 cm^{-1}) along with TiN_x (at 150–300 cm^{-1}) and TiO_2 (rutile) and TiB (at 550–600 cm^{-1}) (see Fig. 4C). VPS Ti/2 vol% hBN also shows the presence of these secondary phases without having no definite hBN peak in the spectrum. However, this doesn't conclude that hBN was not retained after plasma spray in Ti/2 vol% hBN coatings since Raman spectroscopy is location specific and vol% hBN added is very low in the coatings. Further analysis by EDS mapping across the coating cross-section indicates that hBN is retained in the APS Ti/2 vol% hBN coatings (see Fig. 4D). To summarize, the phase analysis revealed that both APS and VPS Ti/2 vol% hBN retained trace amount of hBN after spraying along with hard oxide, nitride, and borides as secondary phases. Ti/10 vol% hBN coatings retained sufficient phase percent of hBN with the addition of secondary phases. The synergistic interaction of retained hBN is expected to improve friction reduction and radiation shielding capacity, while the hard secondary phases are expected to increase the cumulative microhardness and overall abrasive wear resistance of coatings against the lunar regolith particles.

3.4. Microhardness of the composite coatings

The microhardness response of the substrates, pure Ti6Al4V coatings, and Ti6Al4V/hBN composite coatings are shown in Fig. 5. The Al6061 and Ti6Al4V substrates have a microhardness of 106 ± 12 HV and 360 ± 10 HV respectively.

The control samples of pure Ti6Al4V APS coatings have an enhanced microhardness of 39 % compared to the Ti6Al4V substrate and a 326 % improvement compared to the Al6061 substrate. For VPS coatings, this improvement reduces to 184 % for the Al6061 substrate and no improvement for the Ti6Al4V substrate. This improvement is attributed to the formation of metastable TiO phase formed during the APS process. At the same time, VPS control samples also show the presence of the TiO phase, which is not as significant as APS samples due to the vacuum conditions. The microhardness improved by 157 % and 772 % for the APS Ti/2 vol% hBN coatings compared to Ti6 Al4V and Al6061 substrates. This improvement was reduced to 70 % and 527 % for VPS Ti/2 vol% hBN coatings. This significant improvement in cumulative microhardness was attributed to low porosity, uniform melting of powder particles, and the formation of hard secondary phases such as TiO, TiN, and TiB. However, increasing the concentration of hBN to 10 vol% did not improve microhardness further and reduced the improvement compared to Ti/2 vol% hBN coatings. The enhancement in hardness for APS Ti/10 vol% hBN coatings was found to be 466 % and 75 %, while VPS coatings had an enhancement of 390 % and 51 %, respectively, on Al CM and Ti CM substrates. The reduction in hardness for Ti/10 vol% hBN was attributed to the high porosity, non-uniform melting, and defects due to hBN agglomeration. The enhancement in hardness of the composite coatings compared to substrates and control samples is expected to improve the abrasive wear resistance of the coatings against lunar simulant JSC-1 A.

3.5. Tribological performance of the composite coatings

The abrasive wear performance of the substrates and deposited coatings in the presence of JSC-1 A lunar regolith and no-regolith conditions are shown in Fig. 6. The wear rate of the deposited coatings against the substrates proves that all the coatings have enhanced performance in wear rate compared to the Al6061 and Ti6 Al4V substrates (see Fig. 6A). The enhanced microhardness and defect-free nature of the
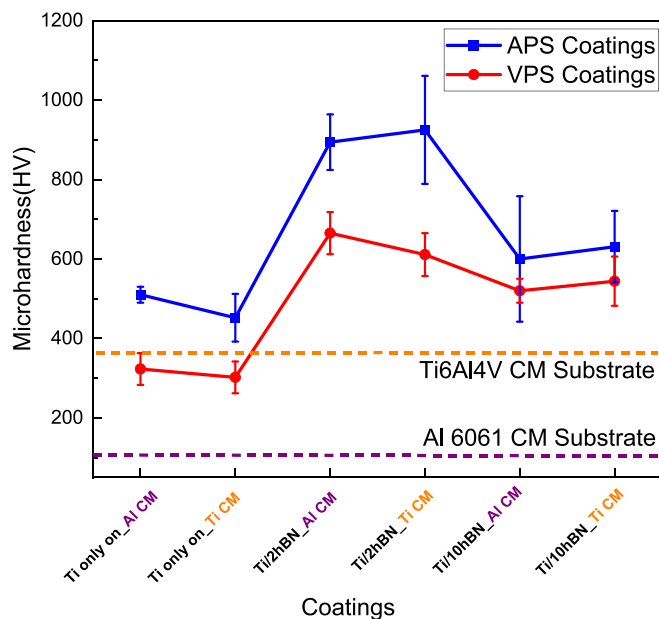

Fig. 5. Microhardness response of the substrates and developed composite coatings.
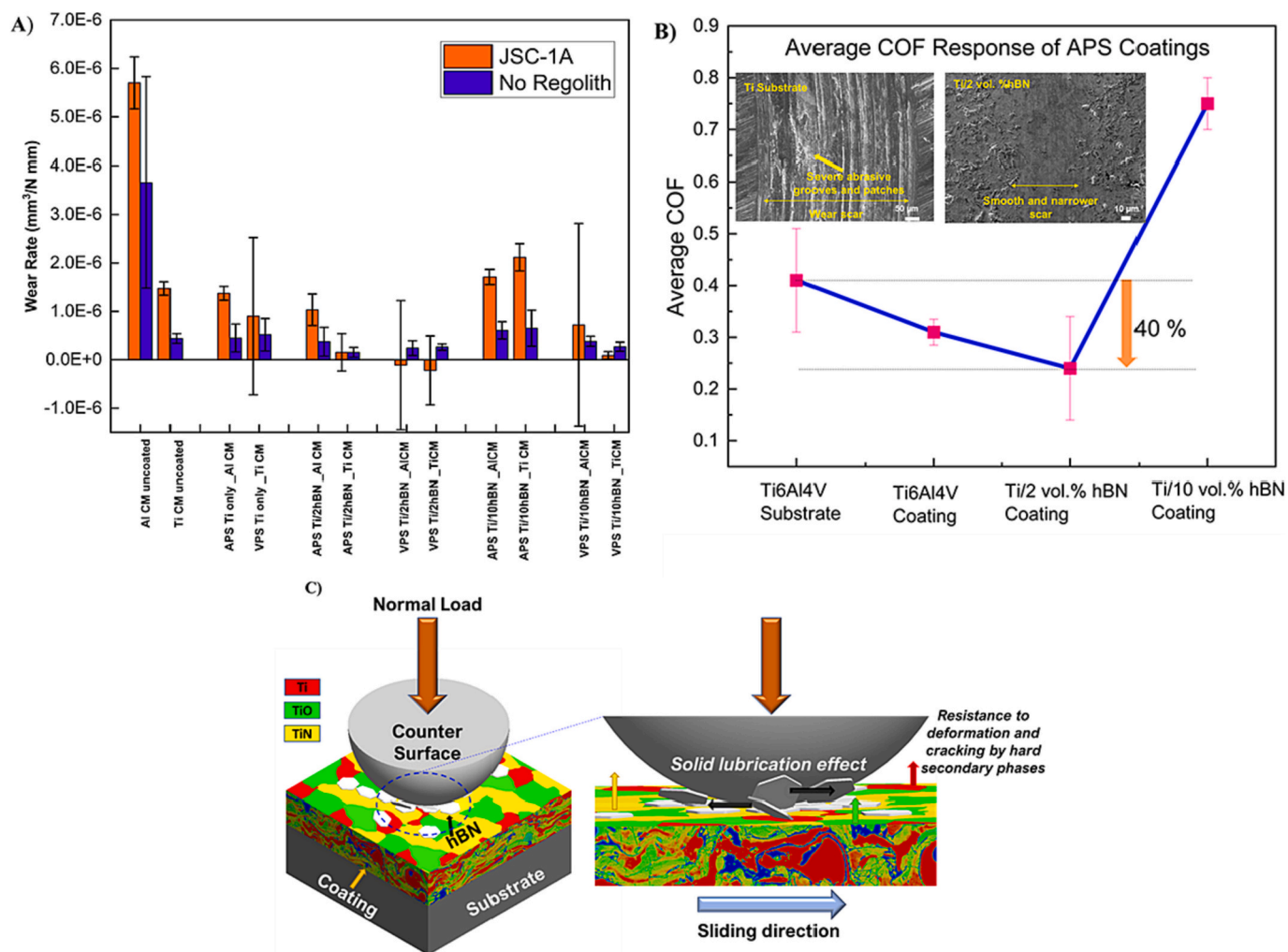
Fig. 6. (A) Wear rate of the composite coatings based on ball-on-disk tribometer tests, (B) Average COF of the composite coatings from ball-on-disk tribometer test in no-regolith condition, and (C) Schematic representation of solid lubrication effect and deformation resistance by the coating layers to improve the wear.

Ti/2 vol% hBN coatings significantly increases the wear rate compared to the pristine substrates. The improvement in wear rate for APS Ti/2 vol % hBN coatings is 90 % and 65 %, respectively, for Al6061 and Ti6Al4V substrates in no-regolith conditions. VPS Ti/2 vol% hBN shows an improvement of 93 % and 40 %, respectively, for the same scenario. In the presence of JSC-1 A lunar regolith, APS Ti/2 vol% hBN shows a significant improvement of 82 % and 90 % for Al6061 and Ti6Al4V substrates. In comparison, VPS coatings show an improvement of 102 % and 114 %, attributed to the minuscule mass gain from embedding JSC-1 A particles.

The enhancement in wear performance is accredited to the synergistic effect of hBN retention in conjunction with the hard secondary phases that increase the cumulative surface hardness of the coatings (see Fig. 6C). The hBN layers shear off upon the applied normal force by the counter surface due to weak van der Waals bonds, which help the layers slide over each other. This produces a solid lubrication effect where the ball slides over the substrate without significant body-body contact. hBN was identified throughout the coating cross-sections due to the uniform coverage of hBN on the Ti powder surface by cryo-milling (Fig. 1C). However, the higher hardness of the coatings limits subsurface layer removal during counter-ball sliding, restricting the interaction of hBN. Fig. 7 indicates smoother and narrower wear scars on coatings compared to substrates. The high hardness of the coatings precedes the solid-lubricity factor on wear enhancement in Ti/2 vol% hBN coatings. Even though the enhancement in microhardness with hBN retention is

observed in the APS Ti/10 vol% hBN coatings, the poor coating integrity resulting from agglomeration, porosities, and unmelted particles results in inferior wear performance compared to 2 vol% hBN coatings and conventional Ti substrate (Fig. 2 C—D, G-H). Compared to the Ti6Al4V substrate, the APS Ti/10 vol% hBN coatings on the Ti substrate have deteriorated the wear performance by 48 % and 44 %, respectively, for no-regolith and JSC-1 A conditions. However, the wear performance for this coating shows an improvement of 83 % and 70 % under no-regolith and JSC-1 A conditions, respectively, when compared to the Al6061 substrate, which is expected due to the high microhardness of Ti6Al4V coatings compared to the Al6061 substrate hardness (See Fig. 5). In contrast, VPS Ti/10 vol% hBN coatings perform better compared to the APS coatings due to the reduction in the concentration of TiO secondary phase to minimize pull-outs from the coating during sliding and having maximum hBN retention in the coatings for solid-lubrication effect. An improvement in wear rate of 39 % and 94 % is observed for the Ti/10 vol % hBN coatings on the Ti6Al4V substrate at no-regolith and JSC-1 A conditions, respectively, while an improvement of 90 % and 87 % is observed for the same coatings on Al6061 substrate. As observed in the case of APS Ti/10 vol% hBN coatings, the VPS coatings also show a slight deterioration in wear performance by increasing hBN to 10 vol%. However, the wear rates are almost identical, and a severe decline in wear performance is not observed. hBN was observed in the wear track for Ti/10 vol% hBN coatings (see Fig. 7E), indicating the solid-lubrication effect and enhanced wear resistance.
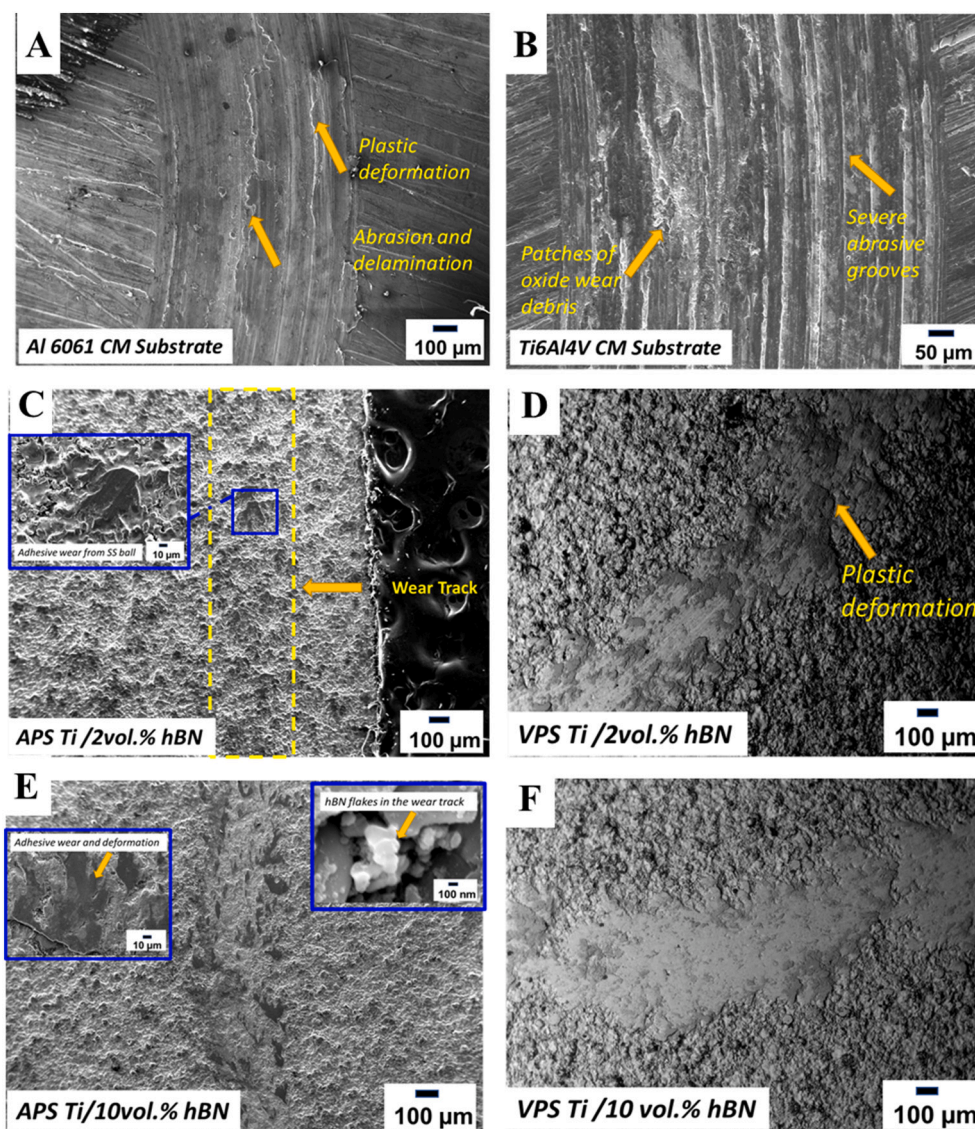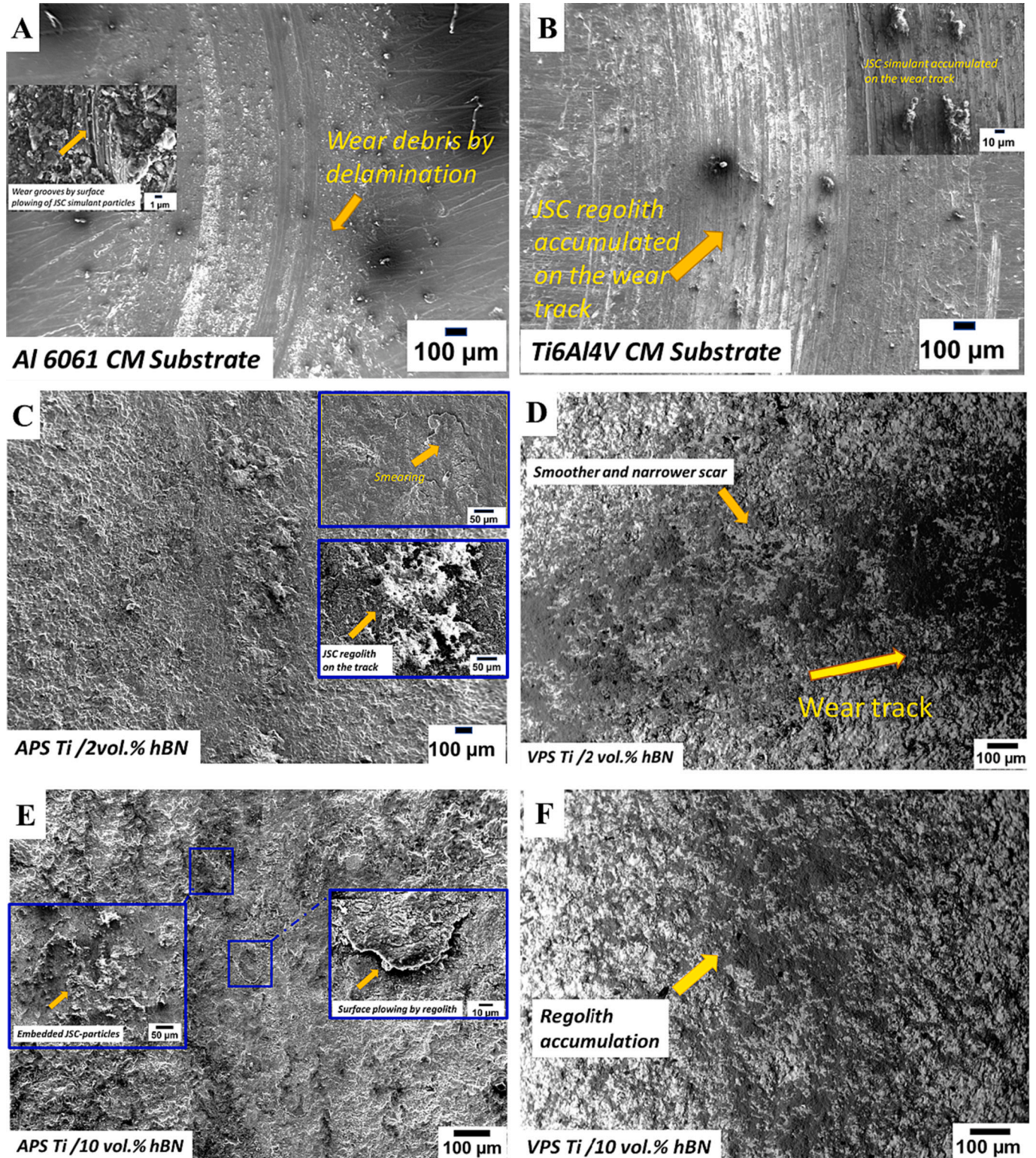
Fig. 7. Top surface worn morphologies of substrates and coatings in the no-regolith test condition: (A) Al 6061 CM substrate, (B) Ti6Al4V substrate, (C) APS Ti / 2 vol% hBN, (D) VPS Ti / 2 vol% hBN, (E) VPS Ti /10 vol% hBN, and (F) VPS Ti /10 vol% hBN.

The average COF response of the substrates and deposited coatings in the no-regolith condition is shown in Fig. S3. In no-regolith conditions, the COF exhibits an increasing trend in the composite coatings due to the enhanced hardness and higher surface roughness compared to the substrates. However, to understand the effect of hBN in COF reduction, the tests were repeated for APS coatings after grinding down to the same roughness. Fig. 6B indicates the plot of average COF against Ti6Al4V substrate and deposited APS coatings in the no-regolith condition. The results show that COF decreases for the Ti/2 vol% hBN coatings by 40 % due to the solid-lubrication effect of hBN. The wear scar profile of Ti6Al4V shows wider and deeper scars with severe abrasive patches and delamination.

In contrast, the Ti/2 vol% hBN coatings offer a smoother and narrower scar devoid of severe abrasion, indicating the superior lubricity of hBN. However, the COF performance also deteriorates with the increase of hBN to 10 vol%, as observed from the case of wear performance. This is attributed to the poor surface integrity of coatings, as explained in the previous sections. When sliding with JSC-1 A, the COF does not indicate a definite trend due to the simultaneous embedding and removal of particles. A slight decrease in the COF by 10 % is observed for the Ti/2 vol% hBN VPS coatings, suggesting hBN retention and associated solid-

lubricity effect. Fig. 7 illustrates the worn morphologies of the top surfaces of substrates and coatings, highlighting the main wear mechanisms involved. Severe abrasion, plastic deformation, and delamination for the Al CM substrate were identified as the primary wear mechanisms [7,60–62] (See Fig. 7A).

On the other hand, the Ti CM substrate exhibited deep abrasive wear grooves with a high density of oxide wear debris, indicating oxidative wear mechanism and adhesive wear [63–65]. Interestingly, the no-regolith abrasive sliding on the Ti/2 vol% hBN coatings did not result in a wear scar track except for isolated patches of adhesive wear caused by the stainless steel (SS) ball used for the ball-on-disk test (see Fig. 7B-D). This was attributed to the very high microhardness of the surface layers of hBN coatings, which countered the action of sliding balls in material removal. EDS analysis of the worn surface of the coatings shows the presence of Fe and Cr, indicating the transfer of material from the SS ball to the coatings (see Fig. S4 A-B, D-E). The wear scars on the coatings revealed an improvement in wear resistance compared to the conventional substrate. However, for the 10 vol% hBN concentration, the reduced microhardness of the coatings led to a slightly predominant scar compared to the 2 vol% hBN coating. Additionally, isolated hBN particles were found across the wear track in the 10 vol% hBN coatings (see

Fig. 7E), indicating that the solid lubrication effect of hBN and higher hardness in the 10 vol% coatings reduce the wear volume loss compared to the pristine substrate material. The primary wear mechanism in the 10 vol% hBN coatings was adhesive wear from SS ball and brittle fracture in isolated areas [66].

When sliding with lunar simulant JSC-1 A, a much higher wear loss was observed on the substrates and coating surfaces than in the no-regolith condition. This was attributed to the contact pressure generated between the mating pairs, causing the simulants to crush under pressure. In addition, the high microhardness of the JSC-1 A simulant (900 HV) enabled particles with sharp edges to plow into the material and remove the surface layers during recurrent sliding. As a result,

Fig. 8. Top surface worn morphologies of substrates and coatings in the JSC-1 A regolith test condition: (A) Al 6061 CM substrate, (B) Ti6Al4V substrate, (C) APS Ti /2 vol% hBN, (D) VPS Ti /2 vol% hBN, (E) VPS Ti /10 vol% hBN, and (F) VPS Ti /10 vol% hBN.

embedding and even covering of regolith are observed on the worn surfaces of both substrates and deposited coatings (See Fig. 8 A-F).

Since the conventional substrates were softer compared to the higher microhardness of the coatings, a higher degree of simulant embedding and plowing into the surface layers were identified using SEM and EDS analysis. EDS revealed the presence of significant elements of JSC-1 A regolith, like aluminum oxide, silicon dioxide, calcium oxide, and magnesium oxide, which were present in the JSC-1 A simulant (see Fig. S4 B—C, E-F). The degree of material removal and embedding was comparatively minimal in the case of the 2 vol% hBN coatings compared to the pristine substrate materials. Fig. 8 A-F shows the worn surface morphologies on the substrates and coatings when sliding in the presence of the JSC-1 A simulant. Severe abrasive wear grooves, micro-cutting, and plowing were observed as wear mechanisms in the pristine substrate materials with several patches of oxide wear debris by simulant. Due to the higher hardness of coatings, the severity of embedding by JSC particles is much lower visually compared to the CM substrates.

The JSC-1 A simulant used in the study has an angular and sharp-edged morphology, with an average size of 36 μm and a broad particle size distribution(see Fig. 9A). Due to its low fracture toughness, the simulant particles fracture and fragment during ball-on-disk sliding, resulting in an average particle size of 25 μm after wear tests. The Ti/2 vol% hBN coatings, which have a higher surface hardness than the ball and comparable microhardness to the simulant particles, fracture the particles during sliding. This produces sharp-edged and angular secondary debris that plows into the coating surface and can cause high wear loss over long test durations. The post-wear debris SEM of the coatings reveals clumps of titanium oxide and titanium debris, as well as micron-sized and fragmented nano-sized hBN flakes (see Fig. 9B). This phenomenon is particularly significant as the coatings are expected to function in harsh lunar environments for at least five to ten years. To study this effect, a panoramic wear scar cross-section analysis was conducted on substrates and coatings to detect regolith embedding and damage. EDS mapping was used concurrently to identify the presence of all core elements. The bare Al CM substrate did not show any embedding under no-regolith conditions. However, sliding with simulants resulted in severe embedding on the wear scar cross-section, as shown in Fig. 9B. The APS Ti/2 vol% hBN coating exhibited isolated regolith embedding areas, which were minuscule compared to the Al/Ti CM substrate due to its high surface hardness (see Fig. 9C).

Comparing the wear performance of various coatings, it is evident that Ti/2 vol% hBN coatings are superior choices irrespective of the thermal spray process. Ti/2 vol% hBN coatings exhibit substantial wear rate improvements compared to Al6061 and Ti6Al4V substrates in no-regolith wear conditions due to their enhanced hardness. In the presence of JSC-1 A lunar regolith, Ti/2 vol% hBN coatings continue to display remarkable enhancements in wear rates for both substrates. The synergistic effect of harder secondary phases and the solid lubrication effect of shearing hBN layers contribute to their wear performance improvement. In contrast, despite enhanced microhardness, APS Ti/10 vol% hBN coatings suffer from poor integrity due to agglomeration and porosities, resulting in inferior wear resistance. VPS Ti/10 vol% hBN coatings perform better than APS coatings due to reduced secondary phase concentration, ensuring solid lubrication with retained hBN. Overall, the Ti/2 vol% hBN coatings, particularly in the presence of JSC-1 A lunar regolith, demonstrate the most promising wear performance, underscoring their suitability for challenging lunar environments. Hence, these coatings can be potential candidates for wear resistance for structural surfaces and moving parts during future lunar surface missions such as landing, excavation, and construction.
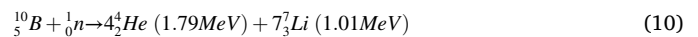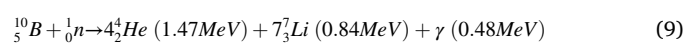
3.6. Radiation shielding performance of the composite coatings

The neutron shielding performance of Ti/hBN composite coatings is determined by the linear absorption cross-section (coefficient, μ_x) and mass absorption cross-section (coefficient, μ_m) based on the Eqs. (2) and (3) are shown in Fig. 10. The enhancement in both mass absorption coefficient and linear absorption coefficient by adding hBN is evident from Fig. 10A. Compared with uncoated Al 6061 CM substrate, both μ_m and μ_x increase by 27 % and 6 % for VPS Ti/2 vol% hBN and Ti/10 vol% hBN, respectively, serve as the best shielding material. This improvement is 7 % and 4 % for APS coatings, respectively. For the Ti6Al4V substrate, the enhancement in μ_m and μ_x increased by 1 % and 7 % for VPS VPS Ti/2 vol% hBN and Ti/10 vol% hBN coatings and 5 % for both APS coatings. This improvement is significant considering that hBN concentration is relatively low (2–10 %) in the 200 μm thick coatings, which is ~3 % of the sample thickness (6.5 mm). The actual hBN concentration in Ti/2 vol% hBN is about 0.06 %, in which the boron content is 0.03 %, and the ^{10}B isotope is only 0.006 % in weight concentration. Yet, the coating still greatly improves radiation shielding for minuscule hBN concentrations. The mass absorption coefficient of the coatings compared to their areal densities is shown in Fig. 10B. The coated samples showed enhanced radiation shielding performance compared to the respective substrates, with VPS coatings showing marginal improvement in mass absorption coefficient against the areal density compared to APS coatings as seen from Fig. 10B.

The higher hBN retention in VPS coatings can be attributed to their lower presence of secondary phases than APS coatings. Conversely, atmospheric oxygen and related reactions during the APS process can hinder hBN retention, leading to lower quantities of hBN in the final coatings. Higher hBN retention in coatings increases shielding effectiveness, owing to the higher percentage of boron atoms and the ^{10}B isotope. Therefore, optimizing coating processes to achieve higher hBN retention is crucial for enhancing neutron radiation shielding capabilities.

The schematic representation of the neutron shielding mechanism of Ti/hBN composite coatings is shown in Fig. 10C. When energized, the neutron source produces thermal neutrons and fast neutrons, depending on the energy level. The titanium and secondary phases in the coatings act as moderators and decelerate the fast neutrons [67]. The boron atoms with a higher neutron absorption cross-section capture and absorb the thermal neutrons more effectively. The capture reactions generate atoms of He and Li, as shown in the following equations [68].

$$^{10}_{5}B + {}^{1}_{0}n \rightarrow {}^{4}_{2}He \, (1.47 MeV) + {}^{7}_{3}Li \, (0.84 MeV) + \gamma \, (0.48 MeV) \tag{9}$$

$$^{10}_{5}B + {}^{1}_{0}n \rightarrow {}^{4}_{2}He \, (1.79 MeV) + {}^{7}_{3}Li \, (1.01 MeV) \tag{10}$$

The thermal energy generated during the reaction process is dissipated through the coating due to the high thermal conductivity of hBN [69]. These reaction products then deposit their energy in the coating material, leading to the reduction of the neutron flux and, thus, the attenuation of the neutron radiation. The hBN content in the composite coatings plays a crucial role in the neutron shielding effectiveness due to the high cross-section of boron atoms for neutron absorption. A secondary phase, such as TiO in the coatings, can hinder the boron atom's ability to absorb neutrons, reducing shielding effectiveness. Therefore, Ti/hBN composite coatings with high hBN content and minimal oxide phases are expected to exhibit high neutron shielding effectiveness.

The space radiation shielding effectiveness of the samples with and without composite coatings was calculated using OLTARIS software under a free space GCR environment. A slab geometry was chosen to arrange the substrate and coating layers, where the coated layer was exposed to the radiation first, similar to the neutron radiation exposure test. Fig. 10D displays the dose equivalent of the samples at each areal density calculated from the actual dimension (density and thickness). The results revealed that the hBN/Ti64 coatings improved the shielding effectiveness (lower dose equivalent) for both Al6061 and Ti64 substrates against GCR despite thin coatings (170–220 μm, 3 % of the substrate thickness) with low boron compositions, which is consistent to the neutron radiation shielding result. It is anticipated that a similar
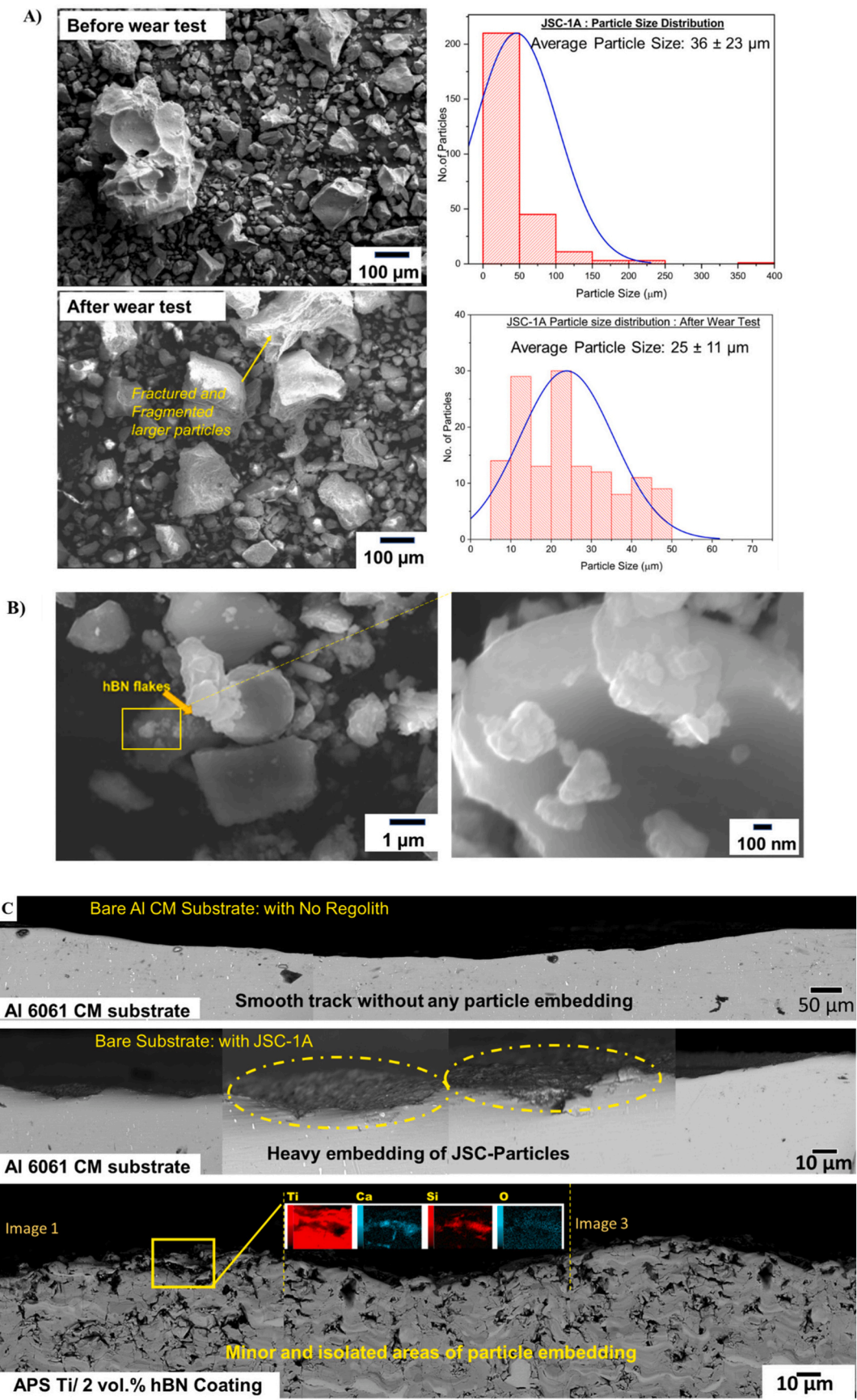
Fig. 9. (A) SEM micrograph and particle size distribution of JSC-1 A simulant particles before and after wear test, (B) SEM micrographs of wear debris morphology from Ti/2 vol% hBN coating and hBN flakes, (C) Panoramic wear scar cross-section imaging with concurrent EDS mapping for bare Al CM substrate without regolith, bare Al CM substrate with regolith, and APS Ti/2 vol% hBN coating with regolith.
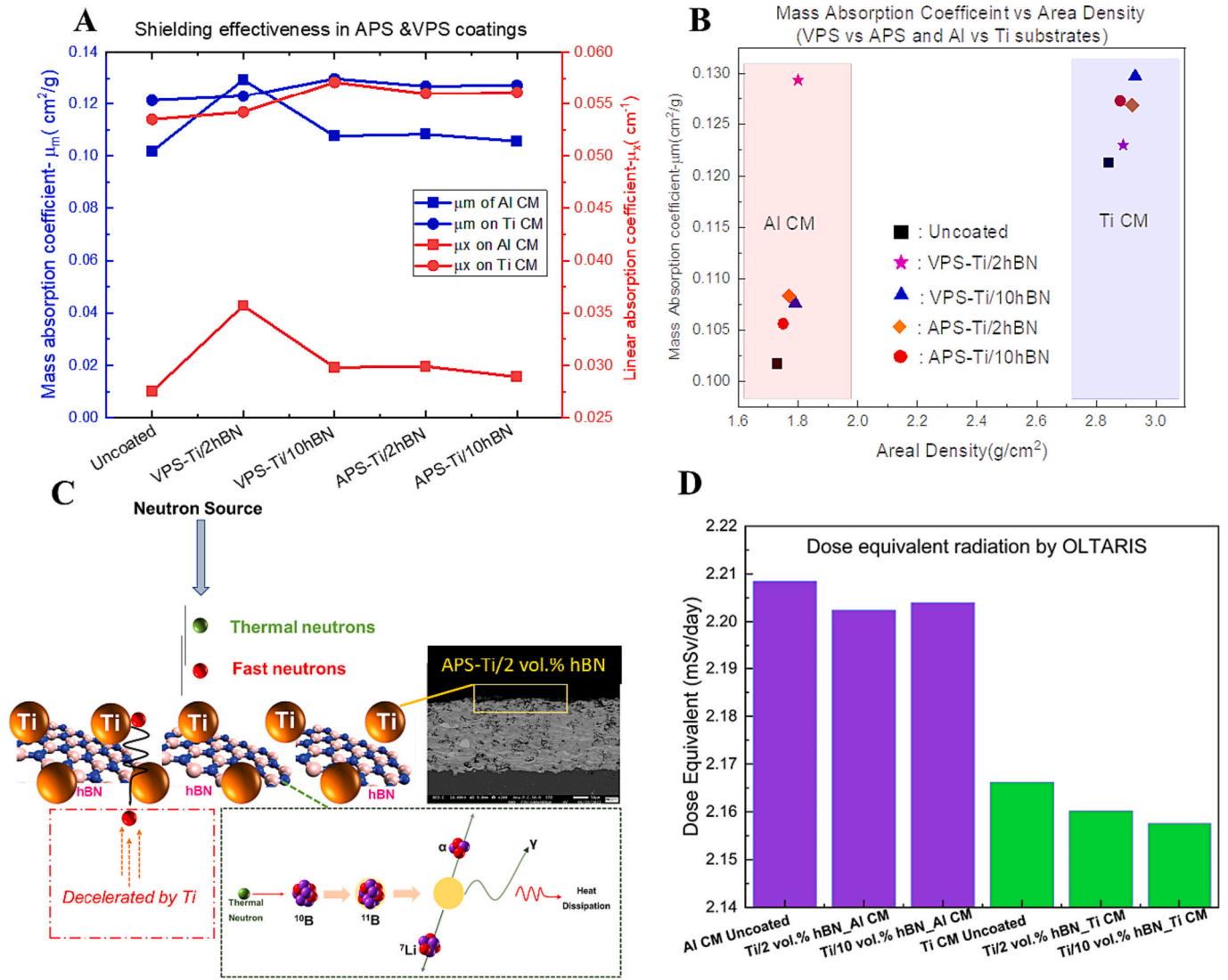
Fig. 10. (A) Radiation shielding response of APS and VPS Ti/hBN composite coatings on Al606 and Ti6Al4V substrates, (B) Mass absorption coefficient vs. areal density for the coatings, (C) Radiation shielding mechanism of Ti/hBN composite coatings, and (D) Dose equivalent of the Ti/hBN composite coatings calculated by OLTARIS under free space GCR environment.

outcome would be observed under a solar particle event (SPE) radiation environment. These results suggest composite coatings can be effective radiation-shielding materials in space applications. Coatings are ranked based on their tribological response against JSC-1 A simulant and neutron shielding effectiveness, as shown in Fig. 11.

Both APS Ti/2 vol% hBN and VPS Ti/10 vol% hBN coatings stand out as the proposed choices for aerospace applications concerning wear and radiation. The synergistic action of hard secondary phases and solid lubricity, high neutron absorption cross-section of retained hBN enhances both wear resistance and shielding effectiveness of the coatings. APS coatings deteriorate under higher hBN concentrations due to agglomeration, defects, and unmelted particles. In contrast, VPS coatings retain the coating integrity by reducing secondary phases and retained hBN provides improved wear and radiation resistance. Hence, these coatings are great candidates for aerospace applications for lunar structural components against challenging environments.

4. Conclusions

The plasma spray (APS & VPS) technique developed multi-functional coatings with improved wear, friction, and radiation properties using
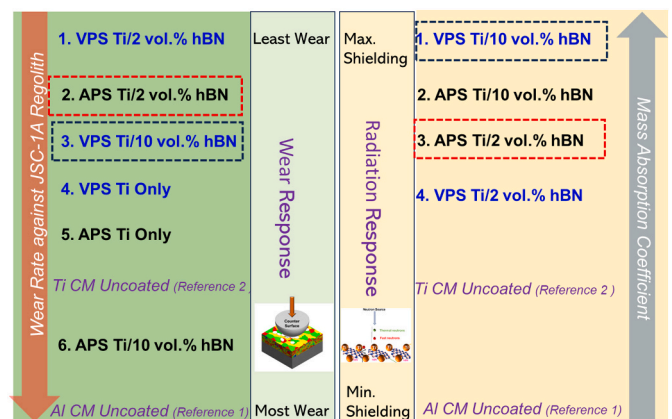

Fig. 11. Rankings of coatings based on the tribological performance against JSC-1 A lunar simulant and neutron shielding effectiveness against Al and Ti substrates.

hBN-reinforced composite powder at 2 and 10-volume percentages. The coating microhardness increased significantly for 2 vol% hBN coatings (~ 3 times) due to the formation of secondary phases such as TiO, TiO_2, and TiN, contributing to the enhancement in mechanical and tribological properties. However, the microhardness of coatings decreased with 10 vol% of hBN due to agglomeration, resulting in weak interfacial bonding and increased porosity. The wear performance improved due to the synergistic interaction of solid lubrication and hard secondary phases in the coatings. The COF friction was enhanced by 40 % for APS Ti/2 vol% hBN coatings compared to Ti substrate. APS and VPS Ti/2 vol % hBN coatings improved the wear performance by 90 % in tests with JSC-1 A lunar simulant, while Ti/10 vol% hBN deteriorated wear enhancement due to hBN agglomeration, porosity, and defects. The wear scar cross-section revealed embedded JSC-1 A particles, which can hamper the performance of structural components. Overall, the Ti/2 vol % hBN coatings, particularly in the presence of JSC-1 A lunar regolith, demonstrate significant enhancements in wear performance, ensuring their suitability for challenging lunar environments.

Radiation shielding results showed that coated samples (APS and VPS) enhanced radiation shielding for minuscule hBN concentrations. An enhancement of 27 % on the mass absorption coefficient was observed for VPS Ti/2 vol% hBN coatings against Al substrates and 7 % against Ti substrates. VPS Ti/2 vol% hBN coatings had a marginal improvement in the mass absorption coefficient against areal density against Al substrates and VPS Ti/10 vol% hBN against titanium substrates. The enhancement in radiation effectiveness of VPS coatings can be attributed to higher hBN retention and lower concentration of oxide phases than APS coatings. Upon a comprehensive comparison and ranking of the various coatings and their respective conditions, it's clear that the APS Ti/2 vol% hBN and VPS Ti/10 vol% hBN coatings are standout options for aerospace applications involving wear and radiation. The study demonstrated that using hBN-reinforced composite powder in plasma spray (APS and VPS) can develop multi-functional coatings with significant wear, friction, and radiation shielding improvements. An optimum between the retained hBN and the second phase must be struck to obtain enhanced wear and radiation properties.

CRediT authorship contribution statement

Abhijith Kunneparambil Sukumaran: Writing – review & editing, Writing – original draft, Methodology, Investigation, Formal analysis, Data curation. **Cheng Zhang:** Supervision, Project administration, Methodology, Investigation, Conceptualization. **Sara Rengifo:** Resources, Project administration, Methodology, Investigation, Funding acquisition, Conceptualization. **Michael Renfro:** Methodology, Investigation, Data curation. **Gia Garino:** Methodology, Investigation, Data curation. **William Scott:** Project administration, Methodology, Investigation. **Matthew Mazurkivich:** Project administration, Investigation, Funding acquisition. **Annette Gray:** Methodology, Investigation, Data curation. **Gabriel Demengehi:** Methodology, Investigation, Data curation. **Ellen Rabenberg:** Methodology, Investigation, Data curation. **Martin Volz:** Methodology, Investigation. **Malik Thompson:** Project administration, Methodology, Investigation. **Brandon Phillips:** Methodology, Investigation. **Nathan Jimenez:** Methodology, Investigation. **Felipe Mora:** Project administration, Methodology, Investigation. **Calista Lum:** Methodology, Investigation, Data curation. **Katie Stephens:** Methodology, Investigation. **Sang-Hyon Chu:** Writing – review & editing, Methodology, Investigation, Formal analysis, Data curation. **Cheol Park:** Writing – review & editing, Methodology, Investigation, Formal analysis. **Arvind Agarwal:** Writing – review & editing, Supervision, Resources, Project administration, Methodology, Investigation, Funding acquisition, Formal analysis, Conceptualization.

Declaration of competing interest

The authors declare that they have no known competing financial interests or personal relationships that could have appeared to influence the work reported in this paper.

Data availability

Data will be made available on request.

Acknowledgments

Appendix A. Supplementary data

Supplementary data to this article can be found online at https://doi.org/10.1016/j.surfcoat.2023.130300.

References

[1] P. Rambabu, N. Eswara Prasad, V.V. Kutumbarao, R.J.H. Wanhill, Aluminium Alloys for Aerospace Applications, 2017, pp. 29–52, https://doi.org/10.1007/978-981-10-2134-3_2.

[2] N.E. Prasad, R.J.H. Wanhill (Eds.), Aerospace Materials and Material Technologies, Springer Singapore, Singapore, 2017, https://doi.org/10.1007/978-981-10-2143-5.

[3] V. Badescu, Moon: Prospective Energy and Material Resources vol. 9783642279690, Springer-Verlag, Berlin Heidelberg, 2013, https://doi.org/10.1007/978-3-642-27969-0.

[4] E.W. Roberts, Space tribology: its role in spacecraft mechanisms, J. Phys. D Appl. Phys. 45 (50) (Dec. 19, 2012), https://doi.org/10.1088/0022-3727/45/50/503001.

[5] E.W. Roberts, M.J. Todd, Space and vacuum tribology, Wear 136 (1) (Feb. 1990) 157–167, https://doi.org/10.1016/0043-1648(90)90078-O.

[6] B. Zhou, B. Liu, S. Zhang, The advancement of 7xxx series aluminum alloys for aircraft structures: a review, Metals (Basel) 11 (5) (May 2021), https://doi.org/10.3390/met11050718.

[7] A.B. Syeda, A. Akhlaq, W. Abdul, M. Abdul, W.H. Syed, Development of lightweight aluminum-titanium alloys for aerospace applications, Key Eng. Mater. 778 (2018) 22–27, https://doi.org/10.4028/www.scientific.net/KEM.778.22.

[8] R.L. Kobrick, Ryan L. Kobrick, PhD Dissertation, 2002.

[9] P. Visscher and D. Woolley, "Midsize Lunar Rover Development and Testing.".

[10] E. T. P. J. DeForce Brian, "Application of Aluminum Coatings for the Corrosion Protection of.".

[11] Z. Gao, Y. He, S. Zhang, T. Zhang, F. Yang, Research on corrosion damage evolution of aluminum alloy for aviation, Appl. Sci. (Switzerland) 10 (20) (Oct. 2020) 1–16, https://doi.org/10.3390/app10207184.

[12] C. Dellacorte, "Nickel-Titanium Alloys: Corrosion 'Proof' Alloys for Space Bearing, Components and Mechanism Applications.".

[13] A.K. Sukumaran, C. Zhang, A. Nisar, S. Rengifo, A. Agarwal, Tribological behavior of Al 6061 and Ti6Al4V alloys against lunar regolith simulants at extreme temperatures, Wear 530–531 (July) (2023) 205028, https://doi.org/10.1016/j.wear.2023.205028.

[14] F. Bouzada, M. Cabeza, P. Merino, S. Trillo, Effect of deep cryogenic treatment on the microstructure of an aerospace aluminum alloy, Adv. Mat. Res. 445 (Jan. 2012) 965–970, https://doi.org/10.4028/www.scientific.net/AMR.445.965.

[15] M. Sutoh, S. Wakabayashi, T. Hoshino, Traveling and abrasion characteristics of wheels for lunar exploration rover in vacuum, J. Terrramech. 68 (Dec. 2016) 37–49, https://doi.org/10.1016/j.jterra.2016.10.002.

[16] D.C. Ferguson, J.C. Kolecki, M.W. Siebert, D.M. Wilt, J.R. Matijevic, Evidence for Martian electrostatic charging and abrasive wheel wear from the wheel abrasion experiment on the pathfinder sojourner rover, J. Geophys. Res. E Planets 104 (E4) (Apr. 1999) 8747–8759, https://doi.org/10.1029/98JE02249.

[17] K.K. Parbatani, V.J. Thomson, Inspection Technique for Reliability Analysis of Lunar Rover Wheel Designs [Online]. Available: http://en.wikipedia.org/wiki/cold_welding#in_space, 2012.

[18] "Rover Wheels - NASA Mars".

[19] https://www.tribonet.org/news/the-next-mars-rover-wheels-designed-to-prevent-wear/.

[20] D.C. Ferguson, et al., The Mars Pathfinder Wheel Abrasion Experiment, 2001.

[21] A. Lama, et al., Macroscale property assessment and indentation characteristics of thick section friction stir welded AA 5083, Mater. Sci. Eng. A 880 (Jul. 2023), https://doi.org/10.1016/j.msea.2023.145306.

[22] D. Dzhurinskiy, A. Babu, S. Dautov, A. Lama, M. Mangrulkar, Modification of Cold-Sprayed Cu-Al-Ni-Al2O3 Composite Coatings by Friction Stir Technique to Enhance Wear Resistance Performance, Coatings 12 (8) (Aug. 2022), https://doi.org/10.3390/coatings12081113.

[23] James R. Gaier, "The effects of lunar dust on EVA systems during the Apollo missions," NASA/TM-2005-213610.

[24] C. J. Wohl, J. W. Connell, Y. Lin, M. A. Belcher, F. L. Palmieri, and B. M. Atkins, "Generation and Evaluation of Lunar Dust Adhesion Mitigating Materials.".

[25] J.P. Williams, D.A. Paige, B.T. Greenhagen, E. Sefton-Nash, The global surface temperatures of the moon as measured by the diviner lunar radiometer experiment, Icarus 283 (Feb. 2017) 300–325, https://doi.org/10.1016/j.icarus.2016.08.012.

[26] F.S. Johnson, J.M. Carroll, D.E. Evans, Vacuum measurements on the lunar surface, J. Vaccum Sci. Technol. 9 (1) (1971) 450–451.

[27] R.V. Kruzelecky, et al., DTVAC Dusty Planetary Thermo-VACuum Simulator Commissioning and LN2 Upgrade, 2018.

[28] S.A. Thibeault, J.H. Kang, G. Sauti, C. Park, C.C. Fay, G.C. King, Nanomaterials for radiation shielding, in: MRS Bulletin vol. 40, no. 10, Materials Research Society, Oct. 08, 2015, pp. 836–841, https://doi.org/10.1557/mrs.2015.225.

[29] W. David, G. R. Olhoeft, and W. Mendell, "Lunar sourcebook: a user's guide to the Moon.".

[30] G. Seisdedos, et al., Assessment and Non-Destructive Evaluation of the Influence of Residual Solvent on a Two-Part Epoxy-Based Adhesive Using Ultrasonics, Appl. Sci. (Switzerland) 13 (6) (Mar. 2023), https://doi.org/10.3390/app13063883.

[31] D. Rickman and K. W. Street, "Some Expected Mechanical Characteristics of Lunar Dust: A Geological View.".

[32] J.E. Colwell, S. Batiste, M. Horányi, S. Robertson, S. Sture, Lunar surface: dust dynamics and regolith mechanics, Rev. Geophys. 45 (2) (Jun. 2007) RG2006, https://doi.org/10.1029/2005RG000184.

[33] P. Metzger, et al., Scaling of Erosion Rate in Subsonic jet Experiments and Apollo Lunar Module Landings, 2010.

[34] R. Nicole Watkins, et al., Lunar Soil Erosion Physics for Landing Rockets on the Moon Growing Plants in Space View project Hydrogen Tape View project LUNAR SOIL EROSION PHYSICS FOR LANDING ROCKETS ON THE MOON [Online]. Available: https://www.researchgate.net/publication/253694116, 2008.

[35] N. S. Land and H. F. Schozz, "SCALED LUNAR MODULE JET EROSION EXPERIMENTS N A S A TN D-505 1.".

[36] N.A. Schwadron, et al., Lunar radiation environment and space weathering from the cosmic ray telescope for the effects of radiation (CRaTER), J. Geophys. Res. Planets 117 (E12) (Dec. 2012), https://doi.org/10.1029/2011JE003978 p. n/a-n/a.

[37] J.W. Wilson, et al., Neutrons in Space: Shield Models and Design Issues, Jul. 2000, https://doi.org/10.4271/2000-01-2414.

[38] J. Köhler, et al., Measurements of the neutron spectrum on the Martian surface with MSL/RAD, J. Geophys. Res. Planets 119 (3) (2014) 594–603, https://doi.org/10.1002/2013JE004539.

[39] L. , T. G. , N. D. , B. T, K.I. Chkhartishvili, Hexagonal boron nitride as a solid lubricant additive (an overview), Nano Studies 14 (2016).

[40] Y. Shang, et al., Multilayer polyethylene/ hexagonal boron nitride composites showing high neutron shielding efficiency and thermal conductivity, Composites Communications 19 (Jun. 2020) 147–153, https://doi.org/10.1016/j.coco.2020.03.007.

[41] L. Du, W. Zhang, W. Liu, J. Zhang, Preparation and characterization of plasma sprayed Ni3Al–hBN composite coating, Surf. Coat. Technol. 205 (7) (Dec. 2010) 2419–2424, https://doi.org/10.1016/j.surfcoat.2010.09.036.

[42] Y. Shang, et al., Multilayer polyethylene/ hexagonal boron nitride composites showing high neutron shielding efficiency and thermal conductivity, Composites Communications 19 (Jun. 2020) 147–153, https://doi.org/10.1016/j.coco.2020.03.007.

[43] R.L. Kobrick, K.G. Budinski, D.M. Klaus, Three-Body Abrasion Testing Using Lunar Dust Simulants to Evaluate Surface System Materials [Online]. Available: http://www.sti.nasa.gov, 2010.

[44] D. She, et al., Abrasive wear resistance of plasma-nitrided ti enhanced by ultrasonic surface rolling processing pre-treatment, Materials 12 (19) (Oct. 2019), https://doi.org/10.3390/ma12193260.

[45] N. Bacca et al., Tribological and neutron radiation properties of boron nitride nanotubes reinforced titanium composites under lunar environment, J. Mater. Res. (Sep. 2022), https://doi.org/10.1557/s43578-022-00708-w.

[46] D.C. Ferguson, J.C. Kolecki, M.W. Siebert, D.M. Wilt, J.R. Matijevic, Evidence for Martian electrostatic charging and abrasive wheel wear from the wheel abrasion experiment on the pathfinder sojourner rover, J. Geophys. Res. E Planets 104 (E4) (Apr. 1999) 8747–8759, https://doi.org/10.1029/98JE02249.

[47] Dongbo Tian, Man Li, Yu Bai, Zhihao Wang, Qiang Yu, and Yu Li, "Abrasion research on axle materials with the influence of simulated lunar dust.".

[48] D. She, et al., Abrasive wear resistance of plasma-nitrided ti enhanced by ultrasonic surface rolling processing pre-treatment, Materials 12 (19) (Oct. 2019), https://doi.org/10.3390/ma12193260.

[49] X. Zhu, Tutorial on Hertz Contact Stress, 2012.

[50] E. Rabinowicz, Friction and Wear of Materials, John Wiley & Sons, Inc., New York, NY, USA, 1965.

[51] C. Fali, C. Junling, Property comparison of vacuum and air plasma sprayed tungsten coatings, J. Alloys Compd. 861 (Apr. 2021), https://doi.org/10.1016/j.jallcom.2020.158422.

[52] Y. Yao, Z. Wang, Z. Zhou, S. Jiang, J. Shao, Study on reactive atmospheric plasma-sprayed in situ titanium compound composite coating, J. Therm. Spray Technol. 22 (4) (Apr. 2013) 509–517, https://doi.org/10.1007/s11666-013-9907-x.

[53] A. Denoirjean, P. Lefort, P. Fauchais, Nitridation process and mechanism of Ti-6Al-4V particles by dc plasma spraying, Phys. Chem. Chem. Phys. 5 (22) (Nov. 2003) 5133–5138, https://doi.org/10.1039/b311186p.

[54] Al-Sabouni, Reactive Plasma Spraying, Cranfield University, 1999.

[55] Y. Yao, Z. Wang, Z. Zhou, S. Jiang, J. Shao, Study on reactive atmospheric plasma-sprayed in situ titanium compound composite coating, J. Therm. Spray Technol. 22 (4) (Apr. 2013) 509–517, https://doi.org/10.1007/s11666-013-9907-x.

[56] H. Zhou, Z. Liu, L. Luo, Microstructural characterization of shrouded plasma-sprayed titanium coatings †, J. Manuf. Mater. Process. 3 (1) (Mar. 2019) https://doi.org/10.3390/jmmp3010004.

[57] P. Kotalík, K. Voleník, Cooling rates of plasma-sprayed metallic particles in liquid and gaseous nitrogen, J. Phys. D Appl. Phys. 34 (4) (Feb. 2001) 567–573, https://doi.org/10.1088/0022-3727/34/4/318.

[58] N.K. Ponon, et al., Effect of deposition conditions and post deposition anneal on reactively sputtered titanium nitride thin films, Thin Solid Films 578 (Mar. 2015) 31–37, https://doi.org/10.1016/j.tsf.2015.02.009.

[59] R. Kaiser, A.N. Christensen, G. Miiller-Vogt, Raman Scattering, Superconductivity, and Phonon Density of States of Stoichiometric and Nonstoichiometric TiN&, 1978.

[60] B. V. Padmini, P. Sampathkumaran, S. Seetharamu, G. J. Naveen, and H. B. Niranjan, "Investigation on the wear behaviour of Aluminium alloys at cryogenic temperature and subjected to cryo-treatment," in IOP Conference Series: Materials Science and Engineering, Institute of Physics Publishing, Jun. 2019. doi:https://doi.org/10.1088/1757-899X/502/1/012191.

[61] S. Bhaskar, S. Athul, G. Premnath, B. Sunil, V.R. Rajeev, Elevated Temperature Wear Behavior of Aluminium Alloy (Al 6061) [Online]. Available: https://www.researchgate.net/publication/328580734, 2018.

[62] D. John, T. Paul, K. Orikasa, C. Zhang, B. Boesl, A. Agarwal, Engineered aluminum powder microstructure and mechanical properties by heat treatment for optimized cold spray deposition of high-strength coatings, J. Therm. Spray Technol. 31 (8) (Dec. 2022) 2537–2559, https://doi.org/10.1007/s11666-022-01455-4.

[63] P. Clayton, Tribological behavior of a titanium-nickel alloy, Wear 162–164 (Apr. 1993) 202–210, https://doi.org/10.1016/0043-1648(93)90502-D.

[64] M. Peters, J. Kumpfert, C.H. Ward, C. Leyens, Titanium alloys for aerospace applications, Adv. Eng. Mater. 5 (6) (Jun. 01, 2003) 419–427, https://doi.org/10.1002/adem.200310095.

[65] T. Kino, S. L. Chen, P. Siitonen, and P. Kettunen, "Densification of Plasma-Sprayed Titanium and Tantalum Coatings.".

[66] A. Anand, M. Das, B. Kundu, V.K. Balla, S. Bodhak, S. Gangadharan, Plasma-sprayed Ti6Al4V alloy composite coatings reinforced with in situ formed TiB-TiN, J. Therm. Spray Technol. 26 (8) (Dec. 2017) 2013–2019, https://doi.org/10.1007/s11666-017-0651-5.

[67] Z. Huo, S. Zhao, G. Zhong, H. Zhang, L. Hu, Surface modified-gadolinium/boron/polyethylene composite with high shielding performance for neutron and gamma-ray, Nuclear Materials and Energy 29 (Dec. 2021), https://doi.org/10.1016/j.nme.2021.101095.

[68] P. Tamayo, C. Thomas, J. Rico, A. Cimentada, J. Setién, J.A. Polanco, Review on neutron-absorbing fillers, in: Micro and Nanostructured Composite Materials for Neutron Shielding Applications, Elsevier, 2020, pp. 25–52, https://doi.org/10.1016/B978-0-12-819459-1.00002-7.

[69] S. Kim, Y. Ahn, S.H. Song, D. Lee, Tungsten nanoparticle anchoring on boron nitride nanosheet-based polymer nanocomposites for complex radiation shielding, Compos. Sci. Technol. 221 (Apr. 2022) 109353, https://doi.org/10.1016/j.compscitech.2022.109353.

[70] A. Sukumaran, C. Zhang, A. Nisar, A. Agarwal, Recent Trends in tribological performance of aerospace materials in lunar regolith environment - A critical review, Adv. Space Res. (2023), https://doi.org/10.1016/j.asr.2023.10.039.

[71] P.R. De Oliveira, A.K. Sukumaran, L. Benedetti, D. John, K. Stephens, S.-H. Chu, C. Park, A. Agarwal, Novel polyimide-hexagonal boron nitride nanocomposites for synergistic improvement in tribological and radiation shielding properties, Tribol. Int. 189 (2023), 108936, https://doi.org/10.1016/j.triboint.2023.108936.

[72] A.K. Sukumaran, A.D. Thampi, E. Sneha, M. Arif, S. Rani, Effect of bovine serum albumin on the lubricant properties of rice bran oil: a biomimetic approach, Indian Acad. Sci. 46 (2021) 207, https://doi.org/10.1007/s12046-021-01717-x.

Tribological and Radiation Shielding Response of Novel Titanium-Boron Nitride Coatings for Lunar Structural Components

Abhijith Kunneparambil Sukumaran[1], Cheng Zhang[1], Sara Rengifo[2], Michael Renfro[3], Gia Garino[1], William Scott[2], Matthew Mazurkivich[2], Annette Gray[2], Gabriel Demengehi[4], Ellen Rabenberg[4], Martin Volz[4], Malik Thompson[5], Brandon Phillips[4], Nathan Jimenez[6], Felipe Mora[7] Calista Lum[8], Katie Stephen[9], Sang-Hyon Chu[10], Cheol Park[10] and Arvind Agarwal [1,*]

[1]Plasma Forming Laboratory, Florida International University, Miami, FL

[2] Materials Test, Chemistry and Contamination Control Branch, National Aeronautics and Space Administration Marshall Space Flight Centre, Huntsville, AL,

[3] Plasma Processes, LLC, Huntsville, AL

[4]Materials Diagnostics and Fracture/Failure Analysis Branch, National Aeronautics and Space Administration Marshall Space Flight Centre, Huntsville, AL

[5]Nonmetallic materials and space environmental effects branch, National Aeronautics and Space Administration Marshall Space Flight Centre, Huntsville, AL

[6]Structural Mechanics Branch, National Aeronautics and Space Administration, Glenn Research Center, Cleveland, OH

[7] Modal Dynamics Test Branch, National Aeronautics and Space Administration Marshall Space Flight Centre, Huntsville, AL

[8]University of California, Irvine, Irvine, CA

[9] University of California, Merced, Merced CA

[10]Advanced Materials and Processing Branch, NASA Langley Research Center, Hampton, VA

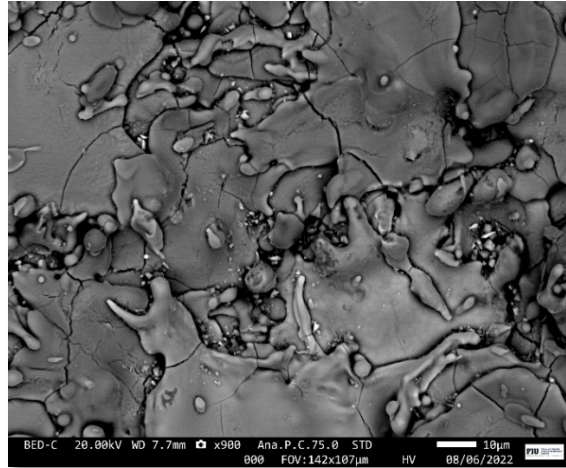[*] Corresponding Author: Arvind Agarwal, agarwala@fiu.edu
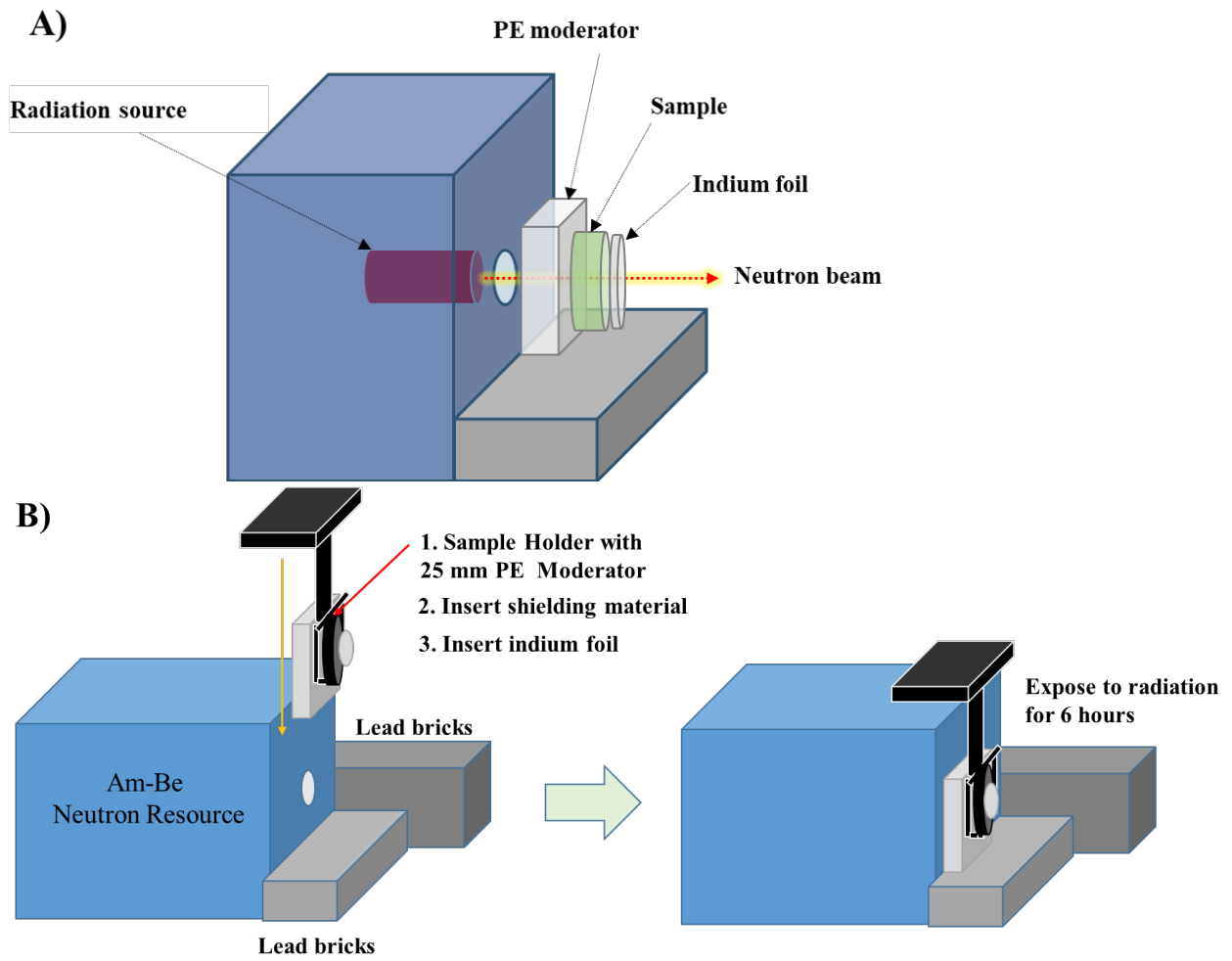
Figure S1: Schematic diagram of A) experimental setup for neutron radiation shielding tests B) operating procedure of radiation testing

(A) Ti-2hBN_Al CM
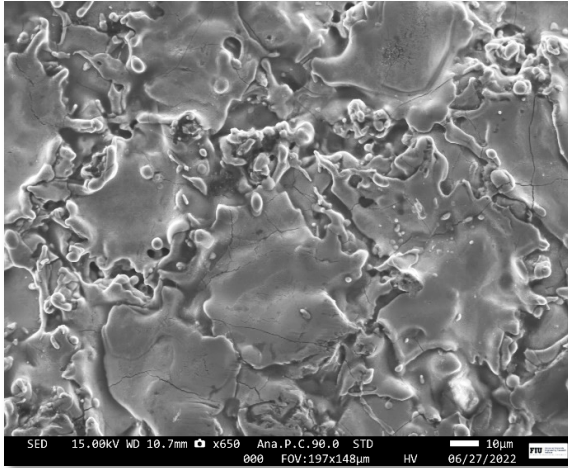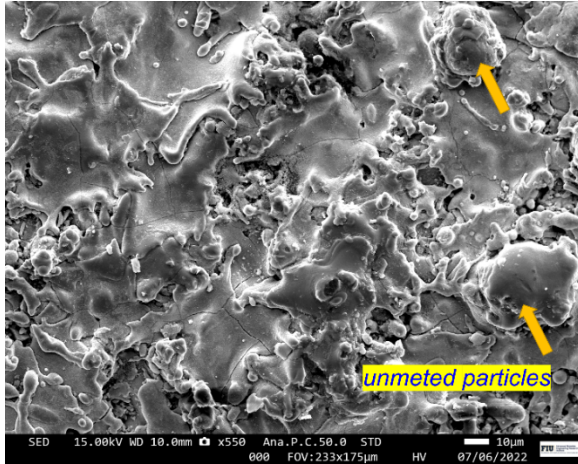

(B) Ti-2hBN_Ti CM

(C) Ti-10hBN_Al CM
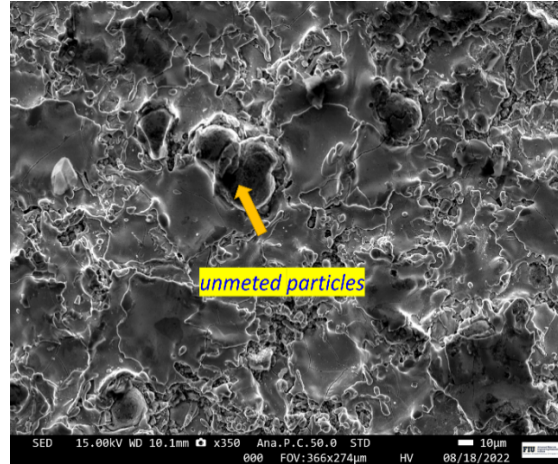

(D) Ti-10hBN_Ti CM

Figure S2: Top surface SEM image of the APS coatings indicates the presence of unmelted particles in the 10 vol.% hBN coatings
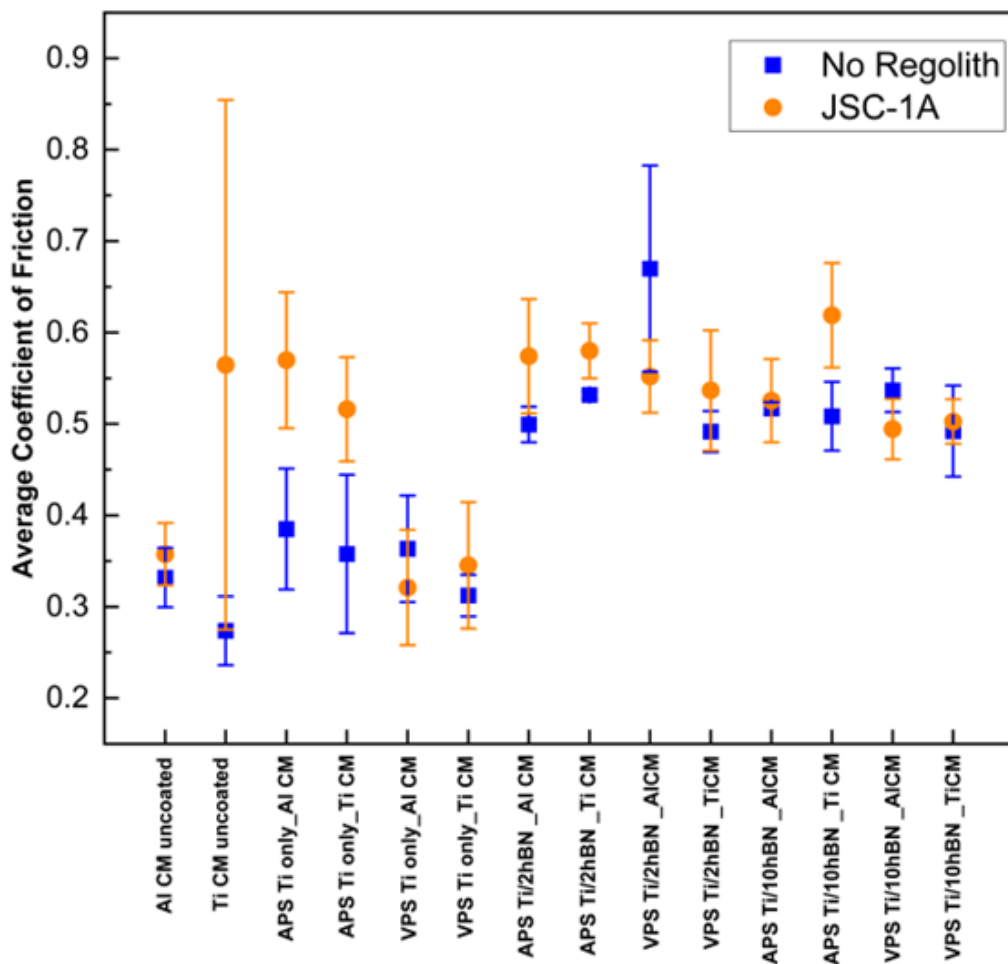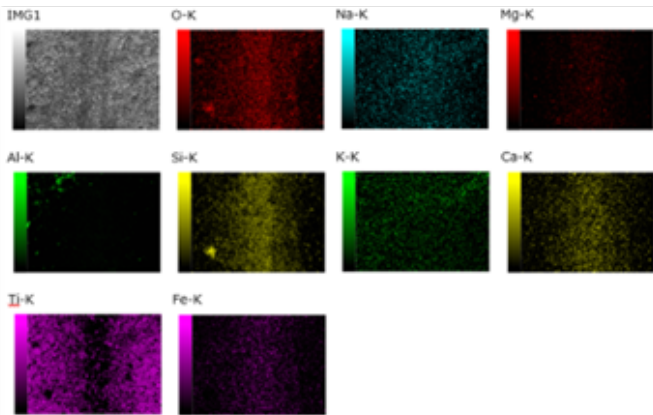
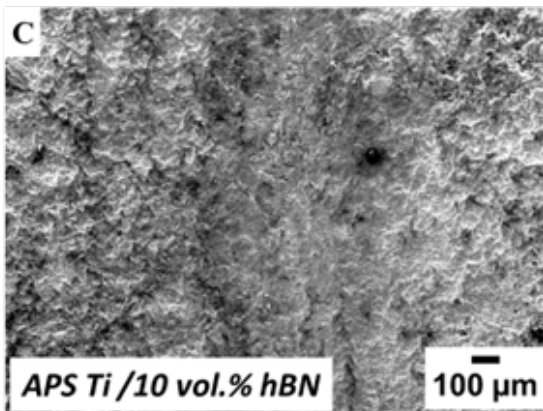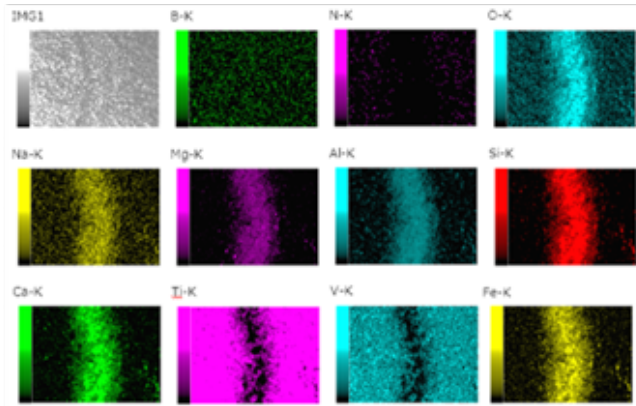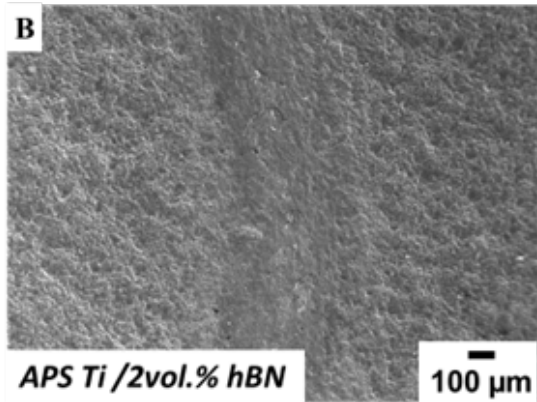**Figure S3:** Average COF of the composite coatings from ball-on-disk tribometer tests.

A — APS Ti /2vol.% hBN — 10 µm

IMG1(1st) | IMG1 | O-K | Al-K | Si-K | Ti-K | Cr-K | Fe-K

B — APS Ti /2vol.% hBN — 100 µm

IMG1 | B-K | N-K | O-K | Na-K | Mg-K | Al-K | Si-K | Ca-K | Ti-K | V-K | Fe-K

C — APS Ti /10 vol.% hBN — 100 µm

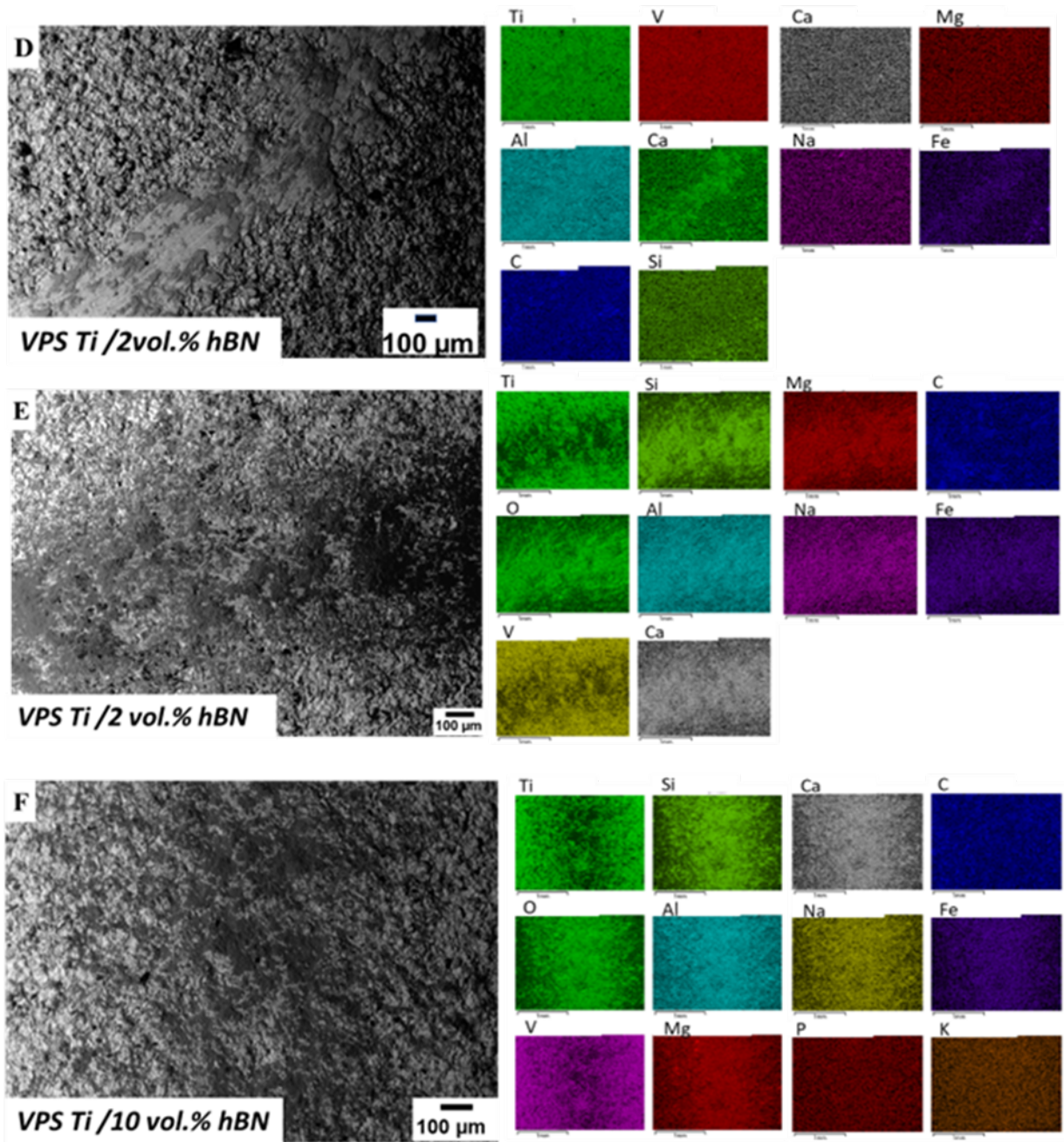IMG1 | O-K | Na-K | Mg-K | Al-K | Si-K | K-K | Ca-K | Ti-K | Fe-K
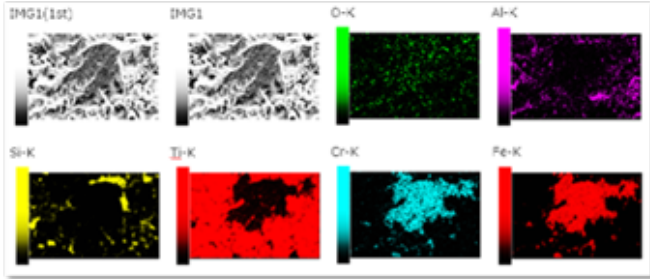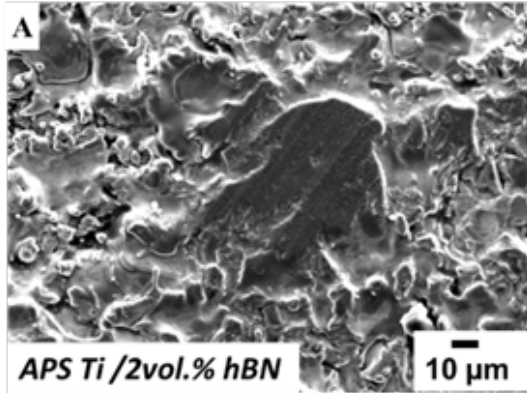
Figure S4: Top surface worn morphologies and corresponding EDS elemental mapping for coatings (A) APS Ti / 2 vol.% hBN in no-regolith condition (B) APS Ti / 2vol.% hBN with JSC-1A (C) APS Ti / 10 vol.% hBN with JSC-1A (D) VPS Ti / 2 vol.% hBN in no-regolith condition (E) VPS Ti / 2 vol.% hBN with JSC-1A (F) VPS Ti / 10 vol.% hBN with JSC-1A. No-regolith tests condition indicating adhesive wear of Fe and Cr from stainless steel ball, JSC-1A condition indicating slight regolith embedding with oxides of Si, Ca, Mg and Al.